The Astrophysical Journal Letters, 968:L11 (23pp), 2024 June 10 https://doi.org/10.3847/2041-8213/ad47fa
© 2024. The Author(s). Published by the American Astronomical Society.
OPEN ACCESS

A Broad Line-width, Compact, Millimeter-bright Molecular Emission Line Source near the Galactic Center

Adam Ginsburg[1], John Bally[2], Ashley T. Barnes[3], Cara Battersby[4], Nazar Budaiev[1], Natalie O. Butterfield[5], Paola Caselli[6], Laura Colzi[7], Katarzyna M. Dutkowska[8], Pablo García[9,10], Savannah Gramze[1], Jonathan D. Henshaw[11,12], Yue Hu[13], Desmond Jeff[1,14], Izaskun Jiménez-Serra[7], Jens Kauffmann[15], Ralf S. Klessen[16,17], Emily M. Levesque[18], Steven N. Longmore[11,19], Xing Lu[20], Elisabeth A. C. Mills[21], Mark R. Morris[22], Francisco Nogueras-Lara[23], Tomoharu Oka[24], Jaime E. Pineda[6], Thushara G. S. Pillai[15], Víctor M. Rivilla[7], Álvaro Sánchez-Monge[25,26], Miriam G. Santa-Maria[1], Howard A. Smith[27], Yoshiaki Sofue[28], Mattia C. Sormani[29,30], Grant R. Tremblay[27], Gijs Vermariën[8], Alexey Vikhlinin[27], Serena Viti[8], Dan Walker[31], Q. Daniel Wang[31], Fengwei Xu[32,33], and Qizhou Zhang[27]

[1] Department of Astronomy, University of Florida, P.O. Box 112055, Gainesville, FL 32611, USA
[2] Center for Astrophysics and Space Astronomy, Department of Astrophysical and Planetary Sciences, University of Colorado, Boulder, CO 80389, USA
[3] European Southern Observatory (ESO), Karl-Schwarzschild-Straße 2, 85748 Garching, Germany
[4] Department of Physics, University of Connecticut, 196A Auditorium Road, Unit 3046, Storrs, CT 06269, USA
[5] National Radio Astronomy Observatory, 520 Edgemont Road, Charlottesville, VA 22903, USA
[6] Max-Planck-Institut für extraterrestrische Physik, Giessenbachstrasse 1, D-85748 Garching, Germany
[7] Centro de Astrobiología (CAB), CSIC-INTA, Carretera de Ajalvir km 4, Torrejón de Ardoz, 28850 Madrid, Spain
[8] Leiden Observatory, Leiden University, P.O. Box 9513, 2300 RA Leiden, The Netherlands
[9] Instituto de Astronomía, Universidad Católica del Norte, Av. Angamos 0610, Antofagasta, Chile
[10] Chinese Academy of Sciences South America Center for Astronomy, National Astronomical Observatories, CAS, Beijing 100101, People's Republic of China
[11] Astrophysics Research Institute, Liverpool John Moores University, IC2, Liverpool Science Park, 146 Brownlow Hill, Liverpool L3 5RF, UK
[12] Max Planck Institute for Astronomy, Königstuhl 17, D-69117 Heidelberg, Germany
[13] Department of Physics, University of Wisconsin–Madison, Madison, WI, 53706, USA
[14] National Radio Astronomy Observatory, 520 Edgemont Road, Charlottesville, VA 22903-2475, USA
[15] Haystack Observatory, Massachusetts Institute of Technology, 99 Milsstone Road, Westford, MA 01886, USA
[16] Universität Heidelberg, Zentrum für Astronomie, Institut für Theoretische Astrophysik, Albert-Ueberle-Str. 2, 69120 Heidelberg, Germany
[17] Universität Heidelberg, Interdisziplinäres Zentrum für Wissenschaftliches Rechnen, Im Neuenheimer Feld 205, 69120 Heidelberg, Germany
[18] Department of Astronomy, Box 351580, University of Washington, Seattle, WA 98195, USA
[19] COOL Research DAO, Germany
[20] Shanghai Astronomical Observatory, Chinese Academy of Sciences, 80 Nandan Road, Shanghai 200030, People's Republic of China
[21] Department of Physics and Astronomy, University of Kansas, 1251 Wescoe Hall Drive, Lawrence, KS 66045, USA
[22] Department of Physics & Astronomy, University of California, Los Angeles, Los Angeles, CA 90095-1547, USA
[23] European Southern Observatory, Karl-Schwarzschild-Strasse 2, 85748 Garching bei München, Germany
[24] Department of Physics, Faculy of Science and Technology, Keio University, 3-14-1 Hiyoshi, Kohoku-ku, Yokohama, Kanagawa 223-8522, Japan
[25] Institute of Space Sciences (ICE, CSIC), Campus UAB, Carrer de Can Magrans s/n, 08193, Bellaterra (Barcelona), Spain
[26] Institute of Space Studies of Catalonia (IEEC), 08860, Barcelona, Spain
[27] Center for Astrophysics | Harvard & Smithsonian, 60 Garden Street, Cambridge, MA 02138, USA
[28] Institue of Astronomy, The University of Tokyo, Mitaka, Tokyo, 181-0015, Japan
[29] Department of Physics, University of Surrey, Guildford GU2 7XH, UK
[30] Università dell'Insubria, via Valleggio 11, 22100 Como, Italy
[31] Department of Astronomy, University of Massachusetts, Amherst, MA 01003, USA
[32] Kavli Institute for Astronomy and Astrophysics, Peking University, Beijing 100871, People's Republic of China
[33] Department of Astronomy, School of Physics, Peking University, Beijing, 100871, People's Republic of China
Received 2024 March 25; revised 2024 April 29; accepted 2024 May 1; published 2024 June 6

Abstract

A compact source, G0.02467–0.0727, was detected in Atacama Large Millimeter/submillimeter Array 3 mm observations in continuum and very broad line emission. The continuum emission has a spectral index $\alpha \approx 3.3$, suggesting that the emission is from dust. The line emission is detected in several transitions of CS, SO, and SO_2 and exhibits a line width FWHM $\approx$ 160 km s^{-1}. The line profile appears Gaussian. The emission is weakly spatially resolved, coming from an area on the sky $\lesssim 1''$ in diameter ($\lesssim 10^4$ au at the distance of the Galactic center, GC). The centroid velocity is $v_{\rm LSR} \approx$ 40–50 km s^{-1}, which is consistent with a location in the GC. With multiple SO lines detected, and assuming local thermodynamic equilibrium (LTE) conditions, the gas temperature is $T_{\rm LTE} = 13$ K, which is colder than seen in typical GC clouds, though we cannot rule out low-density, subthermally excited, warmer gas. Despite the high velocity dispersion, no emission is observed from SiO, suggesting that there are no strong ($\gtrsim$10 km s^{-1}) shocks in the molecular gas. There are no detections at other wavelengths, including X-ray, infrared, and radio. We consider several explanations for the millimeter ultra-broad-line object (MUBLO), including protostellar outflow, explosive outflow, a collapsing cloud, an evolved star, a stellar merger, a high-velocity compact cloud, an intermediate-mass black hole, and a background galaxy. Most of these conceptual

Original content from this work may be used under the terms of the Creative Commons Attribution 4.0 licence. Any further distribution of this work must maintain attribution to the author(s) and the title of the work, journal citation and DOI.

models are either inconsistent with the data or do not fully explain them. The MUBLO is, at present, an observationally unique object.

Unified Astronomy Thesaurus concepts: Galactic center (565); Millimeter astronomy (1061); Millimeter-wave spectroscopy (2252)

1. Introduction

The center of our Galaxy contains billions of stars, tens of millions of solar masses of gas, a supermassive black hole, a tenth of our Galaxy's ongoing star formation, and an extensive graveyard of stellar remnants (e.g., Morris & Serabyn 1996; Henshaw et al. 2023). It is therefore the likeliest place to find new classes of objects. We present one such object in this work.

The following will describe observations (Section 2) and measurements (Section 3) of spectral (Section 3.1), spatial (Section 3.2), spatiospectral (Section 3.3), and continuum (Section 3.4) data, followed by analysis and modeling (Section 4) of the excitation conditions (Sections 4.1 and 4.2), chemistry (Section 4.3), and dust (Section 4.4). We then discuss the location of the source (Section 5), both along the line of sight (Section 5.1) and on the sky (Section 5.2). We engage in extended discussion of the similarities and differences between this object and other classes of objects (Section 6) before concluding that we do not know exactly what this object is (Section 7). Several appendixes present additional spectra (Appendix A), detailed chemical models (Appendix B), and RADEX non–local thermodynamic equilibrium (LTE) models (Appendix C).

2. Observations

The ALMA CMZ Exploration Survey (ACES) large program (2021.1.00172.L; PI: Longmore) observed the central molecular zone (CMZ) with the Atacama Large Millimeter/submillimeter Array (ALMA) in Band 3 (B3). In brief, these data cover six windows: two medium-width windows covering 86–86.5 and 86.7–87.1 GHz, two broad windows covering 97.66–99.54 and 99.56–101.44 GHz, and two narrow windows covering 60 MHz centered on HNCO 4–3 ($\nu_{\rm rest} = 87.925238$ GHz) and HCO^+ ($\nu_{\rm rest} = 89.18852$ GHz). The latter two in particular were shifted to try to cover the full range of velocities of CMZ clouds, since their full bandwidth is only $\sim$200 km s^{-1}. The ACES project covers the whole molecular component of the Galactic Center (GC), spanning roughly $-0.^\circ6 < \ell < 0.^\circ9$ and $-0.^\circ3 < b < 0.^\circ2$ with a total area of 1200 arcmin^2, though in this work, we focus only on the few-arcsecond region around the millimeter ultra-broad-line object (MUBLO). Details of the observational setup are given in Table 1.

The measurement sets were produced by the ALMA pipeline using CASA 6.4.1.12 pipeline 2022.2.0.64; these data were retrieved from the ALMA archive and restored on disk. The data were imaged using CASA 6.4.3–2, adopting the same parameters as used in the original ALMA-delivered pipeline products but with modifications as needed to fix bad cleans (specifically, iterative clean runs that diverged and produced spurious signals) to image windows that were left unimaged because of size mitigation (the two broadband windows were often excluded) or to image those windows with full spectral resolution for the same reason. The continuum data were imaged using the default parameters from the ALMA pipeline, including continuum identification in the UV domain from the ALMA pipeline's `findcont` task. We have combined the ACES 3 mm data with MUSTANG images from Ginsburg et al. (2020) for display purposes in several figures, but all measurements given below are from the ALMA data alone. The full ACES data are still being processed, so as of this publication, we do not yet have a complete census of the broader context.

In this Letter, we focus only on field `aa`, with member observation unit set ID `A001_X15a0_X13c`. During the quality assessment process for the ACES data reduction, we discovered an object with a surprisingly large line width in several spectral lines. We label this a MUBLO, since we do not know its nature beyond its observational properties.

To verify that this feature was not an image artifact (though there was no particular reason to suspect it was), we searched the ALMA archive for overlap with this object. Two programs observing the 50 km s^{-1} cloud, a molecular cloud centered at roughly $\ell = 0.^\circ02$, $b = -0.^\circ08$, $v_{\rm LSR} = 50$ km s^{-1} (Tsuboi et al. 2009), covered this source. Project 2012.1.00080.S (PI: Tsuboi) in B3, which overlaps with the ACES spectral coverage, and 2017.1.01185.S (PI: Mills) in Band 7 (B7), with only the 7 m array, both cover the MUBLO, though it is at the edge of the field in the latter and subject to high noise. We reimaged the archival data from both programs using the ACES pipeline. We note that, while images and cubes were obtained from the 2012.1.00080.S project, and the results below are reasonable, there are some artifacts that persist in that data set that lead us to assign lower credence to differences between those and the ACES data. The problems with the 2012 data set are severe enough that we choose not to show any of the images and strongly caution against interpreting the measurements of these data based only on their statistical errors. Nevertheless, the spectral line measurements from the 2012 data show a few additional detections (see Section 3.1), and the consistent detection of overlapping lines gives us high confidence that the ACES detections are not spurious.

The relevant observational parameters, including uncertainties and beam sizes, are given in Table 1.

3. Measurements

We report measurements of the spectral lines (Section 3.1), the spatial location of both the lines and continuum (Section 3.2), the spatial–spectral structure (Section 3.3), and the continuum (Section 3.4) in this section.

3.1. Spectral

We detect the lines of CS, SO, and SO_2 listed in Table 2. We fitted Gaussian line profiles to the detected lines, and for CS 2–1 and SO 2(3)–1(2), we included foreground absorption components in our models (Figure 1). The line widths are $\sigma = 60$–70 km s^{-1} (FWHM $\sim$ 160 km s^{-1}).

Figures 2 and 3 show spectra of many candidate lines smoothed to 5 km s^{-1} resolution. These spectra are extracted from the peak emission location, i.e., International Celestial Reference System (ICRS) equatorial coordinates $17^{\rm h}45^{\rm m}57.^{\rm s}75$ $-28^\circ57'10.''77$.

Table 1
Data Properties

Data Type	Observation Date	Major ($''$)	Minor ($''$)	PA (°)	rms (mJy beam^{-1})	(Jy K^{-1})	$\nu_{\rm min}$ (GHz)	$\nu_{\rm max}$ (GHz)
Continuum								
(2012.1.00080.S)	2013-05-31T09:52:50.256001	2.359	1.397	86.991	0.4	44.0	85.2491	98.4496
Continuum								
(2017.1.01185.S)	2018-09-27T21:30:24.144000	4.337	2.519	88.344	8.8	0.9	342.2384	357.9871
Continuum spw33+35								
(2021.1.00172.L)	2022-09-15T00:26:52.128000	1.538	1.306	−59.907	0.2	61.4	97.6648	101.4321
Continuum spw25+27								
(2021.1.00172.L)	2022-09-15T00:26:52.128000	1.837	1.468	−70.832	0.2	60.5	85.9664	87.1328
spw25	2022-09-16T00:31:34.272000	1.926	1.573	−71.850	3.1	54.3	85.9664	86.4328
spw27	2022-09-16T00:31:34.272000	1.945	1.566	−72.502	3.2	53.1	86.6665	87.1328
spw33	2022-09-15T00:26:52.128000	1.626	1.440	−52.088	3.4	53.7	97.6648	99.5394
spw35	2022-09-16T00:31:34.272000	1.570	1.293	−67.596	2.6	59.6	99.5619	101.4321

Note. The data types labeled spw*nn* (spw is an abbreviation of spectral window) are from the ACES 2021.1.00172.L data. The 2017.1.01185.S data are from the 7 m array at ALMA, while the other data sets are from the 12 m array.

Table 2
Spectral Line Measurements

Species	Rest Freq (GHz)	Amp (K)	σ_A (K)	Center (GHz)	$\sigma_{\nu,\rm cen}$ (GHz)	$v_{\rm cen}$ (km s^{-1})	$\sigma_{v,\rm cen}$ (km s^{-1})	FWHM (km s^{-1})	$\sigma_{\rm FWHM}$ (km s^{-1})
CS 2–1	97.980950	1.032	0.044	97.9656	0.0010	47.1	3.1	164.5	6.7
SO 2(3)–1(2)	99.299870	1.748	0.025	99.2866	0.0004	40.1	1.1	161.2	2.6
^{34}SO 2(3)–1(2)	97.715317	0.216	0.024	97.7039	0.0026	34.9	8.0	146.8	19.7
SO 2(2)–1(1)	86.093950	0.383	0.026	86.0829	0.0015	38.5	5.3	159.6	12.6
SO_2 2(2,0)–3(1,3)	100.878105	0.172	0.029	100.8748	0.0048	9.9	14.3	173.9	33.6
2012									
C^{34}S 2–1	96.412951	0.139	0.021	96.3966	0.0034	50.8	10.6	139.8	24.9
CS 2–1	97.980950	0.538	0.027	97.9676	0.0011	40.7	3.5	158.6	7.7
^{34}SO 2(3)–1(2)	97.715317	0.129	0.015	97.6974	0.0031	54.8	9.4	168.8	22.1

Note. The columns with σ values give the uncertainty on their neighbors (e.g., σ_A is the uncertainty on the amplitude). All values are from Gaussian fits to the line profile, so the widths are the Gaussian width parameter, not the FWHM.

Table 3
Spatial Measurements

Image	Amp (K)	Amp[mJy] (mJy)	R.A. Off (milliarcsecond)	Decl. Off (milliarcsecond)	Major ($''$)	Minor ($''$)	PA (°)
SO 2(3)–1(2) m0	148.3 (1.1)	2795.0 (21.0)	−149 (5)	4 (5)	1.549 (0.012)	1.816 (0.014)	205.1 (1.9)
					0.85	0.51	−81.16
CS 2–1 m0	55.65 (0.76)	1021.0 (14.0)	−22 (14)	−6 (11)	2.555 (0.035)	1.928 (0.026)	86.0 (1.9)
					2.04	1.17	80.22
CS 2–1 2012 m0	39.36 (0.46)	1459.0 (17.0)	411 (21)	96 (16)	4.34 (0.051)	3.299 (0.039)	95.9 (1.7)
					3.38	2.80	−78.42
Continuum spw33+35	0.1036 (0.0029)	1.77 (0.05)	20 (20)	62 (18)	1.73 (0.049)	1.499 (0.043)	85.3 (8.0)
					0.99	0.43	60.15
Continuum spw25+27	0.1077 (0.0022)	1.758 (0.035)	−55 (16)	149 (15)	1.971 (0.04)	1.783 (0.036)	62.4 (8.2)
					1.22	0.21	33.67
Continuum 2012 cont	0.0906 (0.0031)	1.479 (0.05)	−34 (27)	304 (18)	1.958 (0.066)	1.245 (0.042)	436.3 (2.9)
					…	…	…
Continuum B7	0.0896 (0.0037)	98.2 (4.0)	371 (53)	569 (40)	1.3 (0.13)	0.993 (0.096)	88.3 (6.1)
					…	…	…

Note. The Amp and Amp[mJy] values are in K km s^{-1} and Jy beam^{-1} km s^{-1} for the spectral lines. The R.A. Off. and Decl. Off. columns give offsets from the coordinate $17^{\rm h}45^{\rm m}57.^{\rm s}753$ $-28^{\rm d}57^{\rm m}10.^{\rm s}769$. In the Major, Minor, and PA columns, the alternating rows with no error bars give the beam-deconvolved sizes.

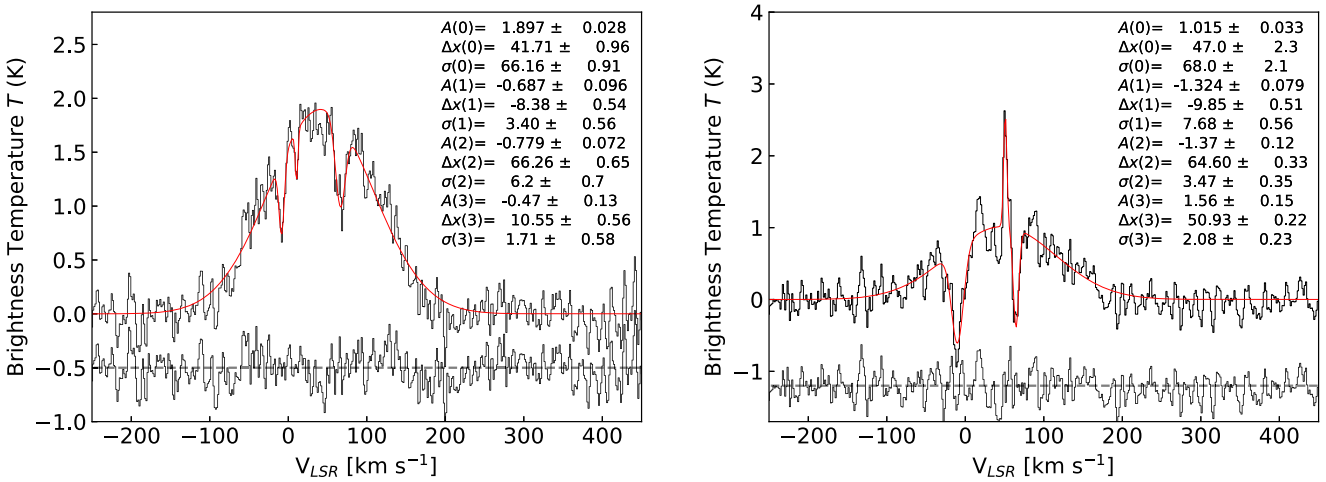

Figure 1. The SO 2(3)–1(2) (left) and CS 2–1 (right) spectra from the ACES data with best-fit models, including narrow absorption and emission features, overlaid. The bottom spectrum shows the fit residual, with the dashed line indicating the zero level. The legend shows the best-fit parameters for the 1D Gaussian function fit, A is the amplitude in K, Δx is the velocity in km s^{-1}, and σ is the width in km s^{-1}.

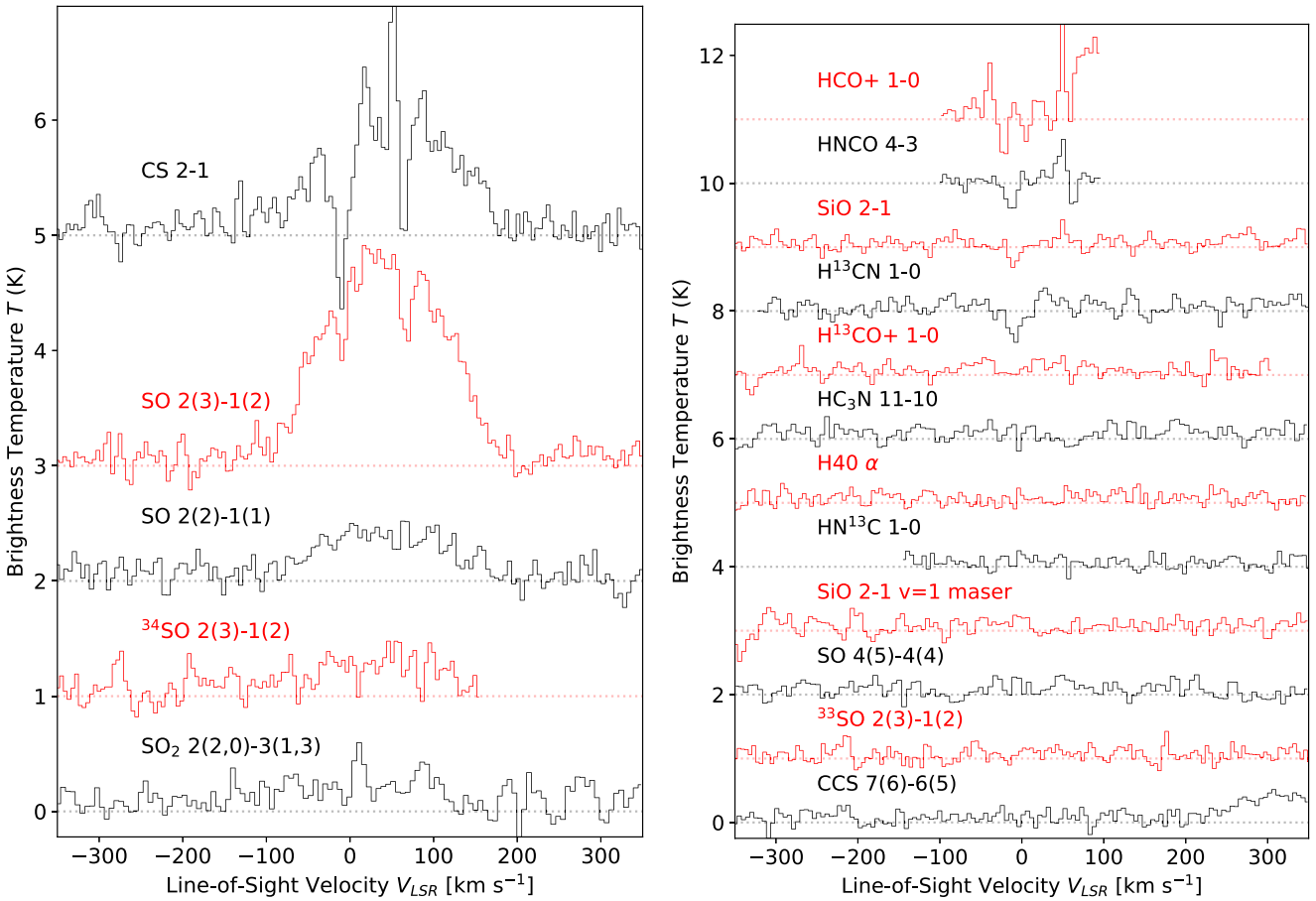

Figure 2. Spectra of detected lines in the ACES spectral coverage (left) and relevant nondetections (right). Only CS, SO, and SO_2 and their isotopologues are detected. Appendix Figure 14 shows the same data with the TP spectra, which cover larger physical scales (∼2 pc), overlaid.

3.2. Spatial

We fitted 2D Gaussian profiles to the continuum and integrated intensity images in all three data sets. The fit parameters from both the continuum and spectral line fits are in Table 3. The uncertainties in this table give only the statistical errors, but all of the spatial measurements are likely affected by systematic errors that are larger; we expect the dominant systematic uncertainty to be from separation between the structured background brightness and the compact Gaussian. While the statistical errors appear to show significant offsets between the different measurements, we regard these as unlikely to be real given the systematic uncertainty.

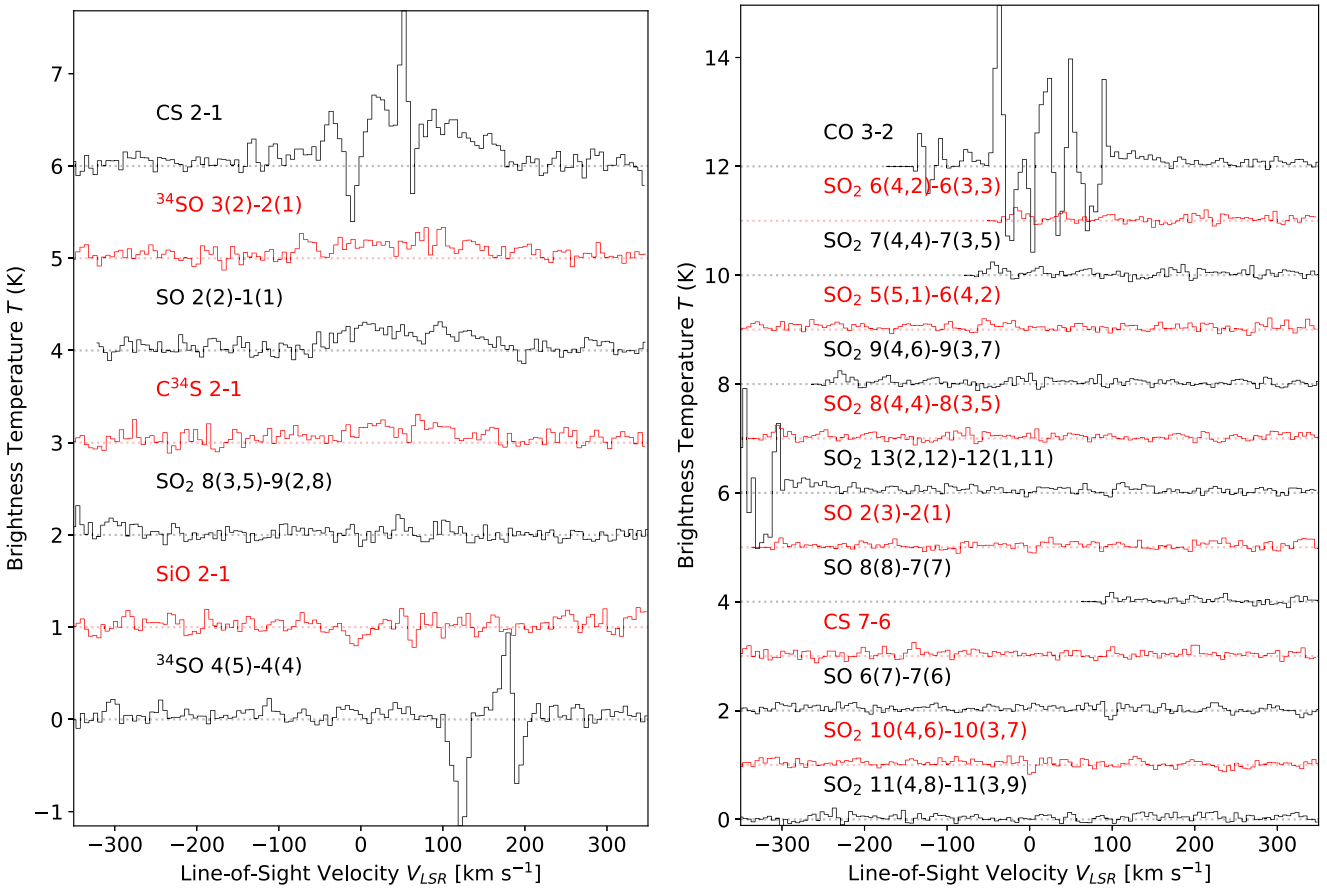

Figure 3. Spectra from 2012.1.00080.S in B3 (left) and 2017.1.01185.S in B7 (right). These show (marginal) detections of ^{34}SO 2(3)–1(2) and ^{34}CS 2–1 in B3 while confirming the clear detections of CS 2–1 and SO 2(2)–1(1). There are no detections in B7. The features in the CO 3-2 spectrum (also seen at the edge of SO_2 13(2,12)–12(1,11)) are from line-of-sight extended features that are poorly reconstructed in the image cube.

Figure 4 shows the 3 mm continuum image from the ACES data alongside the integrated intensity (moment zero) images of CS 2–1 and SO 2(3)–1(2).

3.3. Spatio-spectral

The integrated and peak intensity maps of the detected emission lines are spatially weakly resolved. The deconvolved size is $\sim 1'' \times 0.5''$ (see Table 3).

There is a weak sign of a spatial velocity gradient. We fitted 2D Gaussian profiles to each channel in the SO 2(3)–1(2) cube but found that the fits were too unreliable at the modest signal-to-noise ratio (S/N) in each channel. We therefore collapsed the red (64–152 km s^{-1}) and blue (−68 to 34 km s^{-1}) sides of the cube into moment zero images, excluding an extended cloud that created narrow absorption and emission features around 45 km s^{-1}. Figure 5 shows the result of this fitting. We find that the red and blue sides of the spectrum are spatially separated at $\sim 10\sigma$ significance (and unlike the measurements in Section 3.2, the systematic uncertainties in the red and blue measurements are expected to cancel out). The separation is 2000 ± 200 au assuming $d = 8$ kpc over a 112 km s^{-1} difference, resulting in a gradient of 11,000 km s^{-1} pc^{-1}. Repeating the same measurement with CS 2-1 shows a gradient in the same direction but with a much larger amplitude and lower S/N; the CS measurement was more affected by contamination from extended CMZ clouds.

3.4. Continuum

We detect continuum emission in Bands 3 and 7. Assuming the continuum comes from a single point source, which is consistent with the measurements in Table 3, the spectral index is $\alpha = 3.25 \pm 0.06$ (statistical) ± 0.17 (systematic) (adopting 10% calibration uncertainty), indicating that the emission is coming from dust that is mostly optically thin. Adopting a standard dust opacity for protostellar cores ($\kappa_{100\,\mathrm{GHz}} = 0.002$ cm^2 g^{-1} extrapolated from Ossenkopf & Henning 1994; however, see Section 4.4), assuming $T = 20$ K and a gas-to-dust mass ratio of 100 (so the mass in κ is the total gas+dust mass), we estimate the mass from both frequencies:

$$M = 47\,M_\odot \left(\frac{S_{102\,\mathrm{GHz}}}{1.8\,\mathrm{mJy}}\right)\left(\frac{T}{20\,\mathrm{K}}\right)^{-1} \times \left(\frac{\kappa}{0.002\,\mathrm{cm^2\,g^{-1}}}\right)^{-1}\left(\frac{D}{8\,\mathrm{kpc}}\right)^2, \quad (1)$$

$$M = 35\,M_\odot \left(\frac{S_{350\,\mathrm{GHz}}}{98\,\mathrm{mJy}}\right)\left(\frac{T}{20\,\mathrm{K}}\right)^{-1}\left(\frac{\kappa}{0.018\,\mathrm{cm^2\,g^{-1}}}\right)^{-1} \times \left(\frac{D}{8\,\mathrm{kpc}}\right)^2. \quad (2)$$

The millimeter dust opacity is low, $\tau < 0.01$, at both frequencies. The column density, $N(H_2) \sim 4 \times 10^{23}$ cm^{-2}, corresponds to extinction $A_K \approx 20$. For the B3 source size of

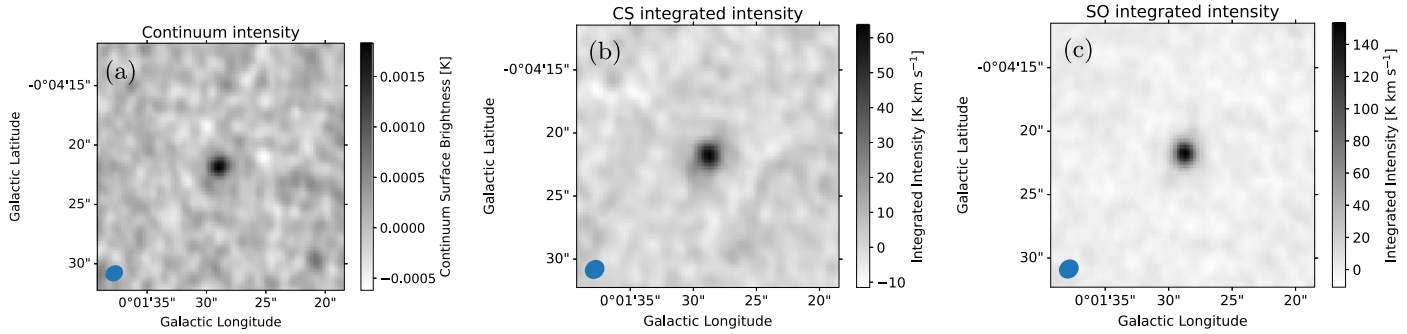

Figure 4. Images of the source at three wavelengths: ACES 3 mm continuum (a), CS 2–1 moment zero (b), and SO 2(3)–1(2) moment zero (c). The moment zero (integrated intensity) images exclude frequencies at which absorption is seen in the line profile or significant extended structure is detected around the source. Moment zero maps showing those velocities, which give a sense of the possible host environment, are shown in Figure 10.

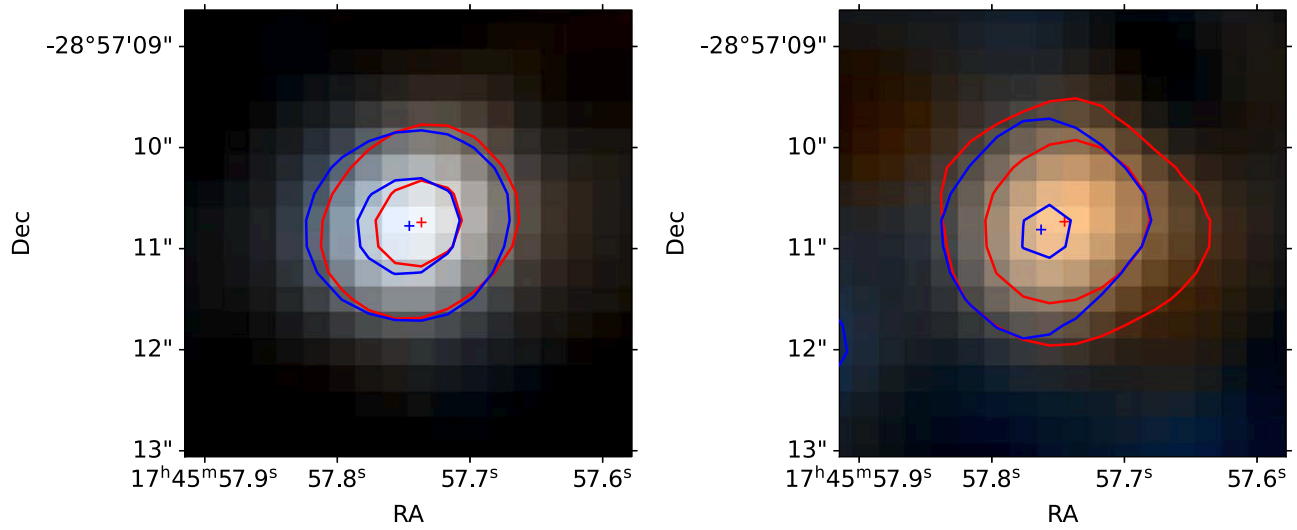

Figure 5. (Left) Moment map made from integrating the red (64–152 km s^{-1}, weighted 104 km s^{-1}) and blue (–69 to +35 km s^{-1}, weighted –8 km s^{-1}) sides of the SO 2(3)–1(2) line profile. Contours are shown at 10σ and 20σ. The plus signs show the 2D Gaussian fit centroids for each moment map. They are separated by 0.5 ± 0.06 pixels (0.″23 ± 0.″03, or 2000 ± 240 au). Both the image and contours show the same data. (Right) Same for CS but with more limited velocity ranges. The centroid separation has the same general direction but is less significant, with a measured offset of 0.″46 ± 0.″12—consistent at the 2σ level. The CS integral was taken from −120 to −20 km s^{-1} on the blue side to avoid contamination from Galactic center clouds, exaggerating the offset and reducing the S/N. The red side is integrated from 75 to 200 km s^{-1}.

$r \approx 5000$ au, assuming spherical symmetry, the molecular number density is $n(\mathrm{H_2}) \sim 10^7$ cm^{-3}. Combining the dust mass with the CS and SO line widths, the energy in the gas is very large, $E_{\rm kin} = 5 \times 10^{48}\ \mathrm{erg}\left(\frac{M}{50\,M_\odot}\right)\left(\frac{\sigma_v}{70\ \mathrm{km\ s^{-1}}}\right)^2$.

We caution that the dust properties assumed above might not be appropriate for all of the types of sources considered in the explanations for the MUBLO discussed in Section 6. Some aspects of nonstandard dust properties are discussed in Section 4.4.

To further constrain the dust properties, we extract limits from multiwavelength data. From the Spitzer (Ramírez et al. 2008; Carey et al. 2009) and Herschel (Traficante et al. 2011) data, we adopt the surface brightness at the position of the source as an upper limit, since in all wavelengths, there is significant extended emission. Table 4 gives the upper limits we determine at each wavelength. Figure 6 shows the spectral energy distribution (SED) with modified blackbody models overlaid. The modified blackbodies are labeled with the adopted temperature in K and column density in cm^{-2} assuming $\beta = 1.5$. For a modified blackbody with a power-

Table 4
SED

Wavelength (μm)	Surface Brightness (MJy sr^{-1})	Beam Area (sr)	Flux (Jy)
3.6	51.613	1.065e-10	0.0055
4.5	62.788	1.065e-10	0.00669
5.8	211.374	1.065e-10	0.0225
8.0	492.624	1.065e-10	0.0525
24.0	1304.027	9.588e-10	1.25
70.0	26,726.094	2.764e-09	73.9
160.0	26,034.621	4.887e-09	127
250.0	12,025.196	1.451e-08	175
350.0	4771.450	2.442e-08	117
500.0	1484.628	4.794e-08	71.2
850.0	299.154	3.283e-10	0.0982
2939.1	18.810	9.412e-11	0.00177
60,000.0	1.481	7.484e-11	0.000111
200,000.0	12.638	4.261e-10	0.00539

Note. Except for the ALMA measurements at 3 mm and 850 μm, these values are upper limits.

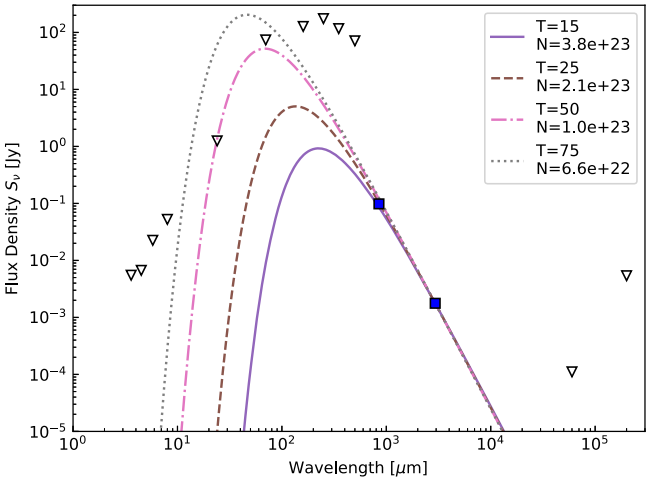

Figure 6. SED of the MUBLO. The data at $\lambda \leqslant 24$ μm are from Spitzer, those from 70 to 500 μm are from Herschel, the millimeter-wavelength data—the detections—are from ALMA, and the longer-wavelength data are from the VLA (Lu et al. 2019) and MEERKAT (Heywood et al. 2022). Triangles indicate upper limits. Four curves are overplotted showing modified blackbody models as described in Section 3.4, with temperature indicated in K and column density in cm^{-2}. All models adopt a dust opacity spectral index $\beta = 1.5$.

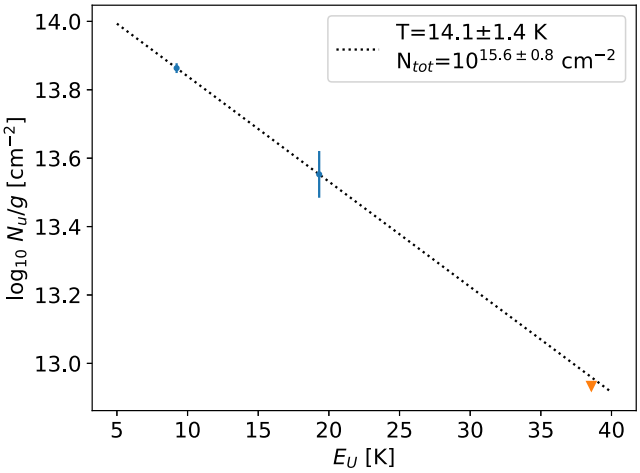

Figure 7. Rotation diagram showing the best fit for the SO lines. The orange point shows the upper limit from the 5(4)–4(4) line.

law opacity function, $\kappa \propto \nu^\beta$, the allowed range of dust temperatures is 15 K $\lesssim T \lesssim$ 50 K: the 850 μm data point sets the temperature lower limit, while the 24 μm and 70 μm upper limits from Spitzer and Herschel data set the temperature upper limits (Figure 6).

4. Analysis

In this section, we attempt to measure the gas temperature by modeling the SO lines under simple conditions (Section 4.1). We then allow for greater complexity in the excitation (Section 4.2) and chemistry (Section 4.3). Finally, we explore the possibility that the dust has atypical properties (Section 4.4).

4.1. LTE Modeling

We detect two transitions of SO with different energy levels and obtain an upper limit on a third, allowing us to make a rotational diagram and fit the temperature and column density assuming LTE conditions, which is reasonable assuming the above density. The temperature from the SO 2(3)–1(2) to 2(2)–1(1) line ratio is $T = 14.1 \pm 1.4$ K (Figure 7; however, see Section 4.2).

We overplot a model emission spectrum based on the LTE fit on the spectral data. Figure 8(a) shows the best-fit model for SO overlaid on the ACES data, and Figure 8(b) shows the model on the 2012 data. In both figures, the CS and SO_2 column densities are scaled to fit the data while assuming the fitted SO rotational temperature. Lines of C^{34}S and ^{34}SO are also detected, giving a ratio ^{32}S/^{34}S $\approx$ 8, consistent with some measurements in the GC (Yu et al. 2020) but inconsistent with others that find ^{32}S/^{34}S $= 16 \pm 4$ (Humire et al. 2020) or 19 ± 2 (Yan et al. 2023). The column density is $N(\mathrm{SO}) = 4 \times 10^{15}$ cm^{-2}. Assuming the same temperature for the other molecules, we obtain column densities $N(\mathrm{CS}) = 10^{15}$ cm^{-2}, $N(\mathrm{C^{34}S}) = 1.2 \times 10^{14}$ cm^{-2}, $N(\mathrm{SO_2}) = 2 \times 10^{16}$ cm^{-2}, and $N(^{34}\mathrm{SO}) = 5 \times 10^{14}$ cm^{-2}. These estimates are dominated by systematic uncertainty in the excitation temperature, which may be more than an order of magnitude. At these column densities, the peak line optical depth is $\tau \sim 0.1$, so the lines are still well approximated as optically thin.

In these same figures (Figure 8), we show model emission lines with the same centroid, line width, and excitation temperature for nondetected lines that we would expect to see in typical molecular and/or shocked gas: H^{13}CO$^+$, H^{13}CN, and SiO. The models correspond to parts of the spectrum with no detection, so they give a rough upper limit on the column densities of these molecules. For H^{13}CO$^+$, the figure appears to show a detection, but this emission comes from the diffuse medium, not the MUBLO.

SO and CS appear to be $\gtrsim$100$\times$ more abundant than H^{13}CO$^+$, H^{13}CN, HC_3N, and SiO. If we adopt the dust-derived column density $N(\mathrm{H_2}) \approx 4 \times 10^{23}$ cm^{-2}, the abundances relative to H_2 are $X_{\mathrm{SO}} \approx 10^{-8}$, $X_{\mathrm{CS}} \approx 2 \times 10^{-9}$, $X_{\mathrm{H^{13}CO^+}} \sim X_{\mathrm{H^{13}CN}} < 5 \times 10^{-11}$, $X_{\mathrm{SiO}} < 10^{-10}$, and $X_{\mathrm{HC_3N}} < 1 \times 10^{-10}$.

4.2. Non-LTE Conditions?

If our mass measurement above is overestimated, the SO lines could be out of LTE, which could significantly change the above abundance and column density calculations.

Non-LTE models confirm the LTE column density estimate. We ran a grid of RADEX (van der Tak et al. 2007) models to test whether non-LTE conditions can match the data. The most useful constraint on the non-LTE physical conditions comes from the intensity ratio of SO 2(3)–1(2)/2(2)–1(1), since this ratio should be mostly unaffected by the unknown filling factor of the emission. Using this measured ratio, $R_{32} = 4.6 \pm 0.3$, and the lower limit on the SO 2(3)–1(2) intensity $S_{32} > 1.75$ K from the filling factor ff $\leqslant 1$, only a narrow range of parameter space is allowed in LTE models: $5 \times 10^{15} < N(\mathrm{SO}) < 2 \times 10^{16}$ cm^{-2} and 5 K $< T <$ 13 K. RADEX one-zone models, adopting $dv = 70$ km s^{-1}, give a wide range of solutions for different temperatures. For example, for $T = 50$ K, the H_2 density can be $10^{2.5}$ cm^{-3} $< n(\mathrm{H_2}) < 10^5$ cm^{-3} for 10^{16} cm^{-2} $> N(\mathrm{SO}) > 10^{15}$ cm^{-2} (see Appendix C). Values of column density >0.5 dex from the LTE model are not allowed even under non-LTE conditions, though the temperature is essentially unconstrained by the RADEX models. However, if we incorporate our estimate of the H_2 number density based on the dust, the non-LTE models are ruled out: all of the high-temperature ($T \gtrsim 20$ K) models require low densities ($n(\mathrm{H_2}) < 10^{5.5}$ cm^{-3}). Additionally, the Meudon photodissociation region (PDR) models

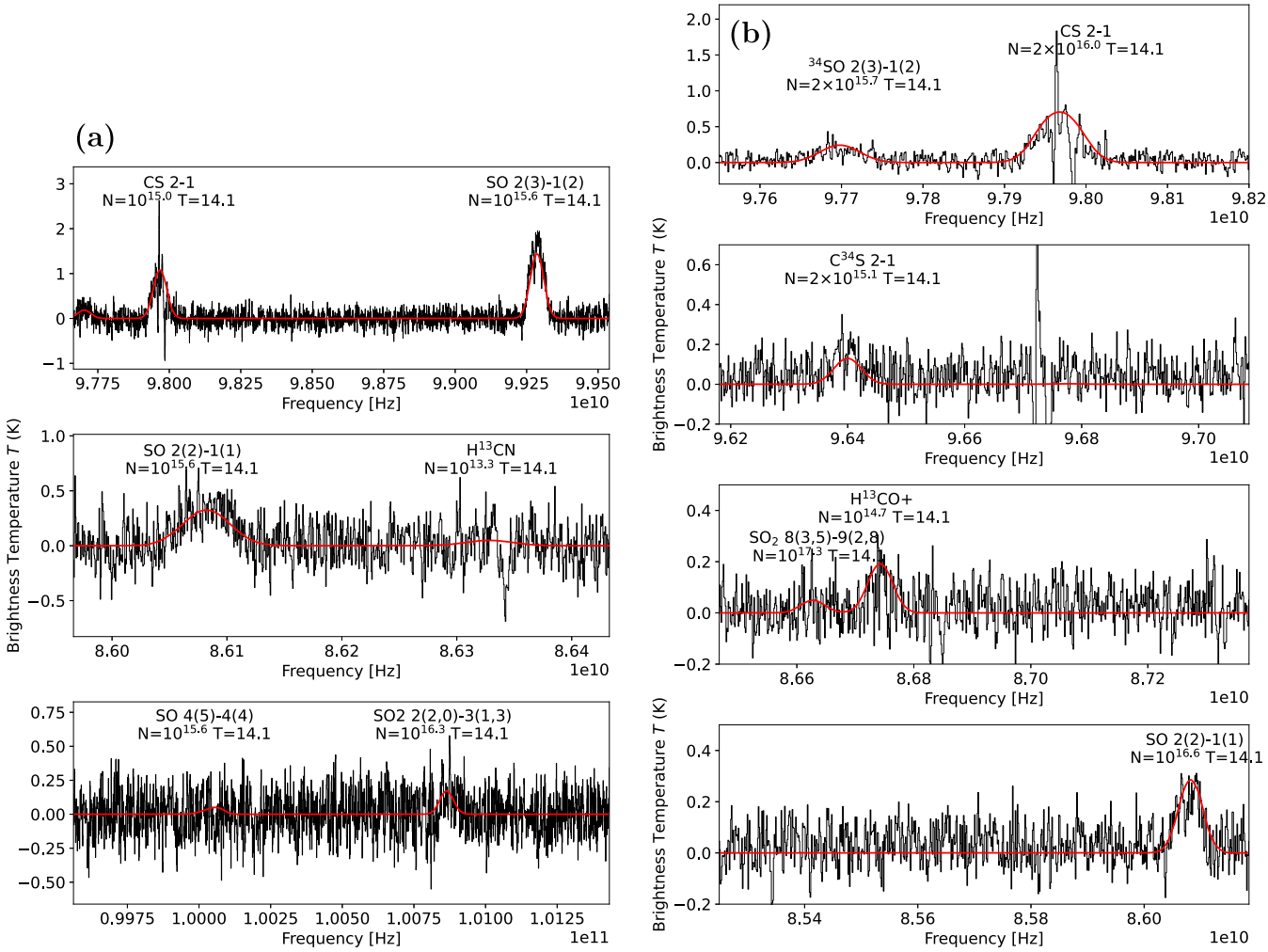

Figure 8. (a) The ACES spectrum. Two detections of SO and one upper limit let us put a constraint on the temperature and column density. The red curve shows an LTE model spectrum with physical parameters shown in the text labels and velocity $v = 41$ km s^{-1}, FWHM = 167 km s^{-1}. (b) The 2012.1.00080.S spectrum. Note that the apparent detection of $H^{13}CO^+$ is not from the MUBLO—while there is emission at this velocity, it is spatially diffuse and not associated with the MUBLO.

that match the low HCN/CS upper limit and the CS/SO ratio require a high density ($n(H_2) \gtrsim 10^7$ cm^{-3}); see Section 4.3 below and Appendix B. We therefore disfavor the non-LTE, low-density model, but additional observations to further test this hypothesis by imaging other SO lines are straightforward and should be performed.

4.3. Chemical Modeling

We have run chemical models to search for physical parameter space consistent with the observations. We ran both Meudon PDR (Le Petit et al. 2006) and UCLCHEM (Holdship et al. 2017) models.

Using the time-dependent gas-grain open-source chemical code UCLCHEM[34] (Holdship et al. 2017), we ran models of a collapsing cloud that varied in final density, UV irradiation, cosmic-ray ionization rate, and temperature. The complete description of the models can be found in Appendix B.2. In brief, there is ample room in the parameter space of radiation field, temperature, density, and cosmic ray ionization rate that produces high SO/SiO ratios (SO/SiO > 100). This ratio is produced by more models for longer time periods at higher densities ($n \gtrsim 10^6$ cm^{-3}) and temperatures ($T \sim 50$ K). With the present data set, these chemical models do not rule out any of the physical models considered below, but they point in constructive directions for what can be observed next to better understand the MUBLO.

We ran Meudon PDR[35] (Le Petit et al. 2006) models spanning a range of extinction, CRIR, density, and UV field (see Appendix B). The Meudon model predicts line intensities in addition to abundances, so we compare to the predicted intensities for these models. The observed line ratio SO 3(2)−2(1)/CS 2−1 can be reproduced at high density ($n_H \sim 10^7$ cm^{-3}) for a wide range of CRIR (10^{-17} s^{-1} $< \zeta_{CR} < 10^{-15}$ s^{-1}). At lower density, $n_H \sim 10^5$, the intensity ratio is at least an order of magnitude below what we observe. The Meudon models therefore favor higher densities and support adopting LTE conditions for SO excitation modeling.

4.4. Weird Dust?

Since we do not know that the dust is protostellar, we evaluate other possibilities. Bianchi & Schneider (2007) adopt

[34] https://uclchem.github.io

[35] https://pdr.obspm.fr/

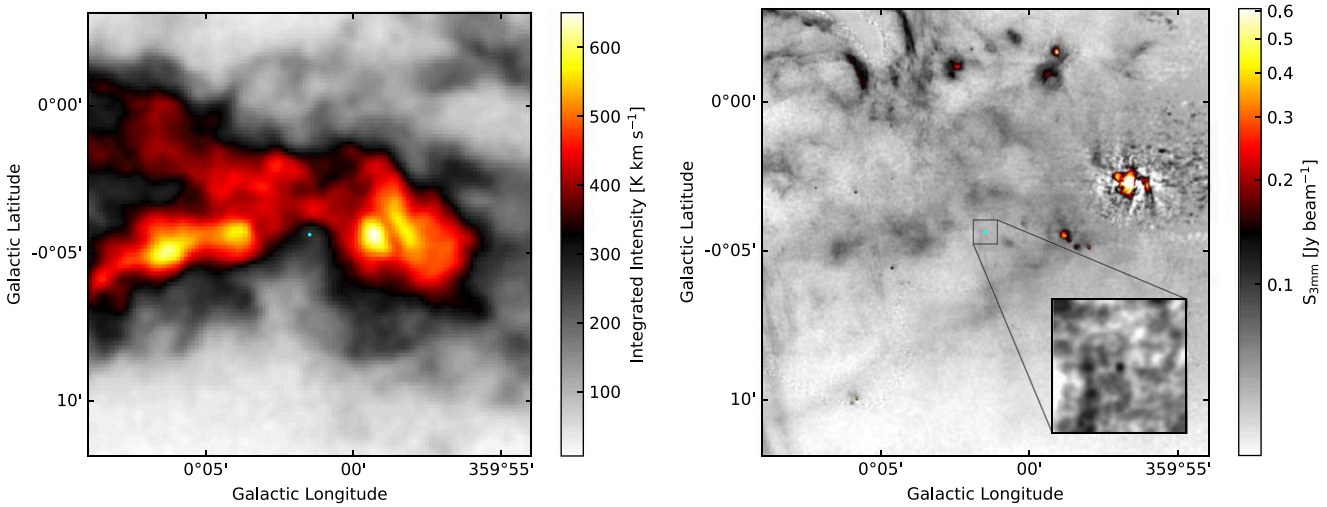

Figure 9. Large-scale images to provide context for the source. The left image shows ^{12}CO integrated intensity from 45 to 55 km s^{-1} from the Nobeyama GC survey (Tokuyama et al. 2019). The MUBLO 3 mm continuum is shown in cyan contours at 40 and 80 mJy beam^{-1} at the very center of the image. The clouds to the left are the "three little pigs" (Battersby et al. 2020), and to the right is the 50 km s^{-1} cloud (Uehara et al. 2019). The right image shows the MUSTANG combined with ACES 3 mm data. The inset shows the same data as the parent image with higher contrast to emphasize the MUBLO. The bright source toward the right is the minispiral, which contains Sgr A*. The arched filaments can be seen in the upper left.

a simple power law for dust in supernovae, which becomes $\kappa_{100\ \mathrm{GHz}} = 0.4\left(\frac{100\mu\mathrm{m}}{3\mathrm{mm}}\right)^{1.4} = 0.0034\ \mathrm{cm}^2\ \mathrm{g}^{-1}$, a factor of 2 larger than we assumed; supernova dust would be only marginally different from our assumptions. Following Kamiński (2019), who modeled dust in the circumstellar envelope of evolved star VY CMa, we extrapolate the Draine & Lee (1984) opacities to be $\kappa_{102\ \mathrm{GHz}} = 0.00032$ and $\kappa_{350\ \mathrm{GHz}} = 0.0040$. If the dust is like that in VY CMa, the mass is substantially (∼5×) larger than we reported. Draine (2006) gives a range of dust opacities of $0.0003\ \mathrm{cm}^2\ \mathrm{g}^{-1} < \kappa_{102\ \mathrm{GHz}} < 0.03\ \mathrm{cm}^2\ \mathrm{g}^{-1}$, where the large end of this range corresponds to carbonaceous dust (pyrolized cellulose) that is too opaque to comprise a significant amount of the interstellar medium (ISM). If the dust is comprised primarily of carbon, the mass may be as much as 15× smaller than we reported, a mere 2 $M_\odot$ of gas, though this possibility is especially unlikely given the large column density of SO and SO_2 detected, which indicates that the medium is not especially carbon-rich.

In all of the above measurements, we have adopted a standard gas-to-dust ratio of 100. If we were looking at a hydrogen-free object, comprised entirely of dust, the mass would be quite small, merely ∼0.5 $M_\odot$. Such tötally mëtal objects have been suggested to be possible to assemble in the turbulent ISM (Hopkins 2014), but there is no immediate reason to expect it to exhibit extreme line widths.

Reservoirs with ∼0.5 $M_\odot$ in dust alone have been inferred in some supernova remnants (SNRs) and evolved stars. Kamiński (2019) suggests that the envelope of VY CMa might contain 0.5 $M_\odot$ of dust (see also Section 6.2 below), but (as Kamiński 2019 points out) this value is uncertain because of the substantial optical depths involved in this calculation. Chawner et al. (2019) infer dust reservoirs of 0.3–0.5 $M_\odot$ in pulsar wind nebulae based on Herschel data. Given stellar masses of $\ll 10^2\ M_\odot$ that produced these quantities of dust, there must be gas-to-dust mass ratios of $\ll 10^2$, higher dust opacities than assumed in the respective analysis, or both. Such work demonstrates that, under certain conditions, continuum emission at an intensity seen in the MUBLO can be produced by gas reservoirs well below the nominal value of $M_{\mathrm{gas}} \sim 50\ M_\odot$ from Section 3.4.

5. Where Is It?

While the MUBLO is seen in projection close to the GC, only 5′ from Sgr A*, its line-of-sight location has to be determined. In this section, we cover the evidence that it is genuinely in the GC, likely 10–100 pc from Sgr A*.

5.1. Line-of-sight Location

The line-of-sight velocity $v_{\mathrm{LSR}} \approx 40$–$50$ km s^{-1} is similar to other GC objects. There are absorption lines seen in front of the broad lines, and these are clearly from GC gas based on their continuity with clouds that are definitely in the CMZ (the "three little pigs" and the 50 km s^{-1} cloud). Assuming these are genuine absorption features and not interferometric artifacts (it remains difficult to be entirely certain that all interferometric artifacts have been removed, even when working with combined 12 m + 7 m + total power, TP, data), the source cannot be in the foreground of the CMZ. These absorption features are discussed further in Appendix A, which shows the ACES single-dish TP data extracted from the same position overlaid on the spectrum we have already shown from the 12 m data. While it is clear that the MUBLO is behind these GC clouds, it is possible that it could be in the far side expanding 3 kpc arm (Dame & Thaddeus 2008), which exists at a similar velocity.

5.2. Spatial Location

Figure 9 shows where the MUBLO resides in the large-scale context of the CMZ, showing both CO and 3 mm continuum images. On these larger scales, the MUBLO resides in an underdensity or cavity in the CO gas (Tokuyama et al. 2019). Figure 10 shows the object in its local context from the ACES data, indicating that there is surrounding molecular gas but that this gas is not particularly associated with the MUBLO. The gas seen in Figure 10 is sparser than in the neighboring dense

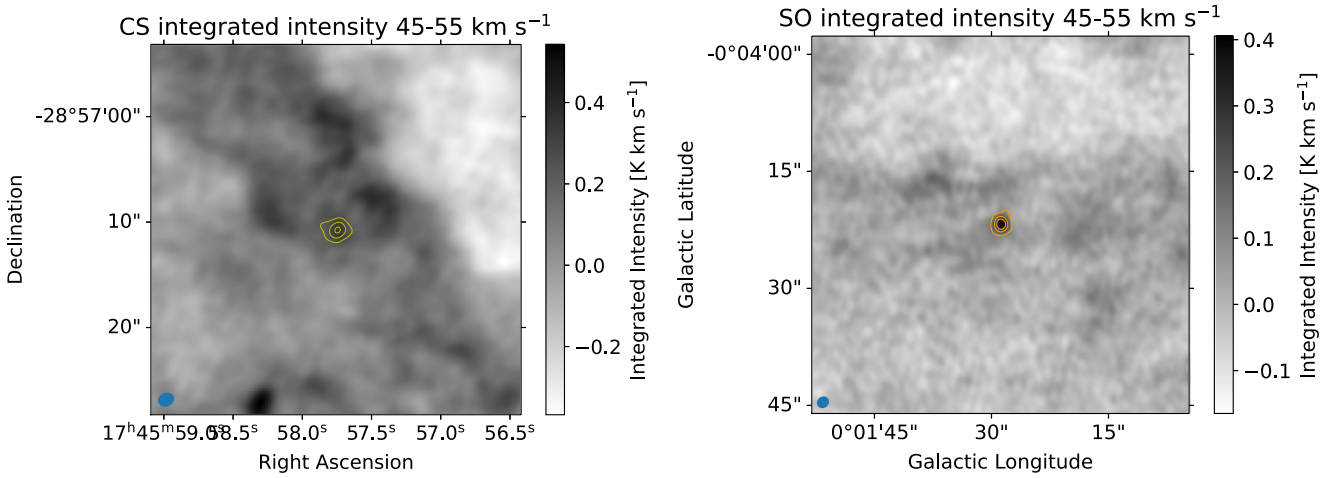

Figure 10. In both images, the gray scale shows the integrated intensity over the range 45–55 km s $^{-1}$. The left image shows CS 2–1, and the right shows SO 2(3)–1(2). The contours show the MUBLO integrated over the full velocity range but with contaminated velocities masked out; the contours are at 20, 40, and 60 K km s^{-1} (CS; left) and 20, 60, and 100 K km s^{-1} (SO; right). These images provide context on where the compact source resides. The MUBLO is not detected in CS over the narrow velocity range because the "diffuse" molecular gas at that velocity dominates over the compact source, while the MUBLO is still well detected in SO over the same velocity range, presumably because the SO 1(2) level (the lower state of the SO 2(3)–1(2) transition) is un- or underpopulated in the diffuse cloud.

clouds seen in Figure 9; it is the wispy edge of the clouds seen on the larger scales.

We next check multiwavelength archival data for any counterparts to this source. Figure 11 shows contours from the ACES data overlaid on high-resolution near-IR images from the GALACTICNUCLEUS (Nogueras-Lara et al. 2018, 2019) and Hubble Space Telescope (HST) (Dong et al. 2011) surveys. No source is evident in the near-IR data at the location of the MUBLO. If anything, there is a hint of a deficit of flux at the position of the MUBLO in the HST images, which could be caused by the dust extinguishing background sources. Archival images from the Hubble Legacy Archive in the F127M, F139M, and F153M filters show this feature more distinctly (Whitmore et al. 2016). We also checked the surrounding sources from Shahzamanian et al. (2022) within $r < 10''$ and saw no obvious pattern in the proper motions of nearby sources that might indicate a recent runaway or a particularly deep potential well. We searched Vizier (Ochsenbein et al. 2000) for any public catalogs with a source at this location at any wavelength and found no compelling counterparts. The closest sources listed in any catalog are $>1''$ away, and these can readily be seen to be outside the contours of the MUBLO in Figure 11.

We further checked longer-wavelength data. Figure 12 shows this source in context, with cutouts of the GLIMPSE (Churchwell et al. 2009), MIPSGAL (Carey et al. 2009), HiGal (Molinari et al. 2010), Very Large Array (VLA) *C*-band (Lu et al. 2019), and MEERKAT (Heywood et al. 2022) surveys. The only detections are with ALMA at 3 and 0.85 mm. This source is unfortunately not covered by the millimeter-wavelength survey CMZoom (Battersby et al. 2020).

No X-ray sources are present at this location. The closest cataloged source is $>7''$ away (Muno et al. 2009). We have examined recently taken Chandra X-ray data (Vikhlinin et al. 2024, in preparation) comprising 708 ks effective integration at this location. The 3σ upper limit is $<2.8 \times 10^{-5}$ counts s^{-1} in the 3–8 keV band, equivalent to $S_X < 7 \times 10^{-16}$ erg s^{-1}cm^{-2} assuming a $\gamma = 2$ power-law spectrum.

6. What Is It?

We have demonstrated the existence of a dusty, broad-line-width source that is detected only at millimeter wavelengths. Given this limited information, we now attempt to classify the object.

We consider many options. Plausible mechanisms include protostellar outflow, explosive outflow, protostellar inflow, ejecta from an evolved star, a planetary nebula (PN) or pre-planetary nebula (PPN), stellar collision, a high-velocity compact cloud (HVCC), an intermediate-mass black hole (IMBH), a galaxy, or a supernova. We evaluate each of these hypotheses in the following sections but find that none satisfactorily explain the data.

6.1. Something Associated with Star Formation

Star formation is prevalent in the GC, with roughly 10% of the Galaxy's star formation occurring in the central $r < 100$ pc (Longmore et al. 2013; Barnes et al. 2017; Henshaw et al. 2023). We therefore evaluate several hypotheses associated with star formation. Star-forming regions are naturally dust- and molecule-rich. We consider whether the MUBLO is a protostar (Section 6.1.1), a typical protostellar outflow (Section 6.1.2), an explosive outflow (Section 6.1.3), a protostellar inflow (Section 6.1.4), a protostar collision (Section 6.1.5), or a prestellar core collision (Section 6.1.6). While these hypotheses can explain some of the bulk properties of the MUBLO, they all fail in the details, particularly energetics, morphology, and chemistry.

6.1.1. Protostar

Before digging into the specific models to explain the gas, we evaluate what kind of central source is allowed by the observed dust SED described in Section 3.4. Using the Richardson et al. (2024) update to the Robitaille (2017) grid, we searched for models consistent with either of the two ALMA millimeter detections (we did not require that both measurements match the models since the model grid does not allow for a varying β parameter). We search for models that

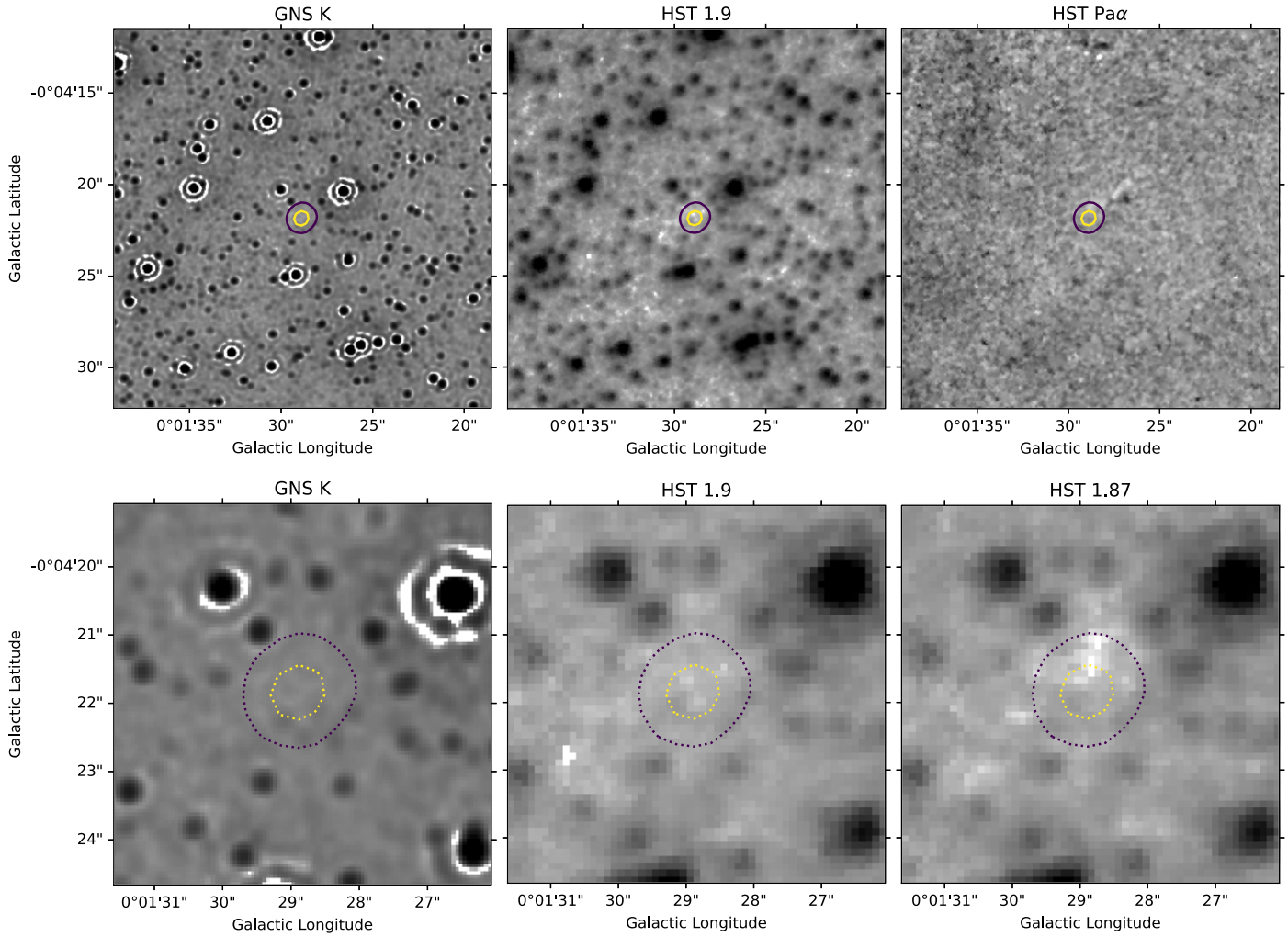

Figure 11. Near-infrared continuum images with millimeter continuum contours from the ACES 12 m data overlaid at 40 and 80 mK. (Top row) Left is the *K*-band image from GALACTICNUCLEUS (Nogueras-Lara et al. 2018, 2019), middle is the F190 filter from the HST, and right is the F187–F190 Paschen α from HST (Dong et al. 2011). All are shown with darker colors indicating brighter emission. There is a hint of Paα absorption on the north end of the source and just to the northwest of the source, but it is unclear how much to trust these; the bright star to the northwest may produce the apparent absorption as an artifact of the continuum subtraction. (Bottom row) The left and middle panels are the same, just zoomed further in. The right panel is the HST F187 filter, which is the narrow band that contains the Paα line.

have a flux density within 5000 au apertures matching the ALMA measurements to within 25% and falling below the 24 and 70 μm upper limits. There is a narrow range of parameter space compatible with the ALMA measurements and Herschel and Spitzer upper limits, all with $10^4\,L_\odot < L < 10^{4.7}\,L_\odot$ and $3\,M_\odot < M_{\rm gas}(<5000\,{\rm au}) < 28\,M_\odot$. While these objects are part of the model grid, they are not compatible with most models of star formation, since the implied central source is an $M \gtrsim 10\,M_\odot$ star that is surrounded by a comparable amount of cold gas in a stable envelope-plus-disk configuration. Instead, these models demonstrate that there exist solutions in which high-luminosity, but still $L < 10^5\,L_\odot$, stars may be embedded in dusty envelopes that produce enough millimeter-wavelength emission while not exceeding the short-wavelength limits.

6.1.2. Protostellar Outflow

The hypothesis that the object is a protostellar outflow from a previously unknown star-forming region is plausible. However, there is a good deal of evidence that suggests that this is not the correct interpretation.

1. The limited number of emission lines detected, and especially the lack of SiO, would make this outflow unlike any others in the Galaxy. Admittedly, our sensitivity to CO is limited, since it was only covered in the coarse spatial resolution B7 data such that diffuse molecular gas along the line of sight is confused with and may absorb any compact emission associated with the MUBLO.
2. It is surprisingly compact, $<10^4$ au, which suggests that it is almost perfectly face-on (any angle would produce an extended, red/blue bipolar signature). Similarly, the small value of the spatial gradient with velocity suggests that it is face-on. This situation is unlikely but possible.
3. The line profile is Gaussian. Such a profile is unexpected for a straight-on outflow, which would more likely include some sharper features or flattening from the high-velocity tails. However, if the material we observe is entirely entrained ISM, a Gaussian profile is not impossible.
4. Assuming this is a face-on outflow-driving source, we would expect to see the central young stellar object

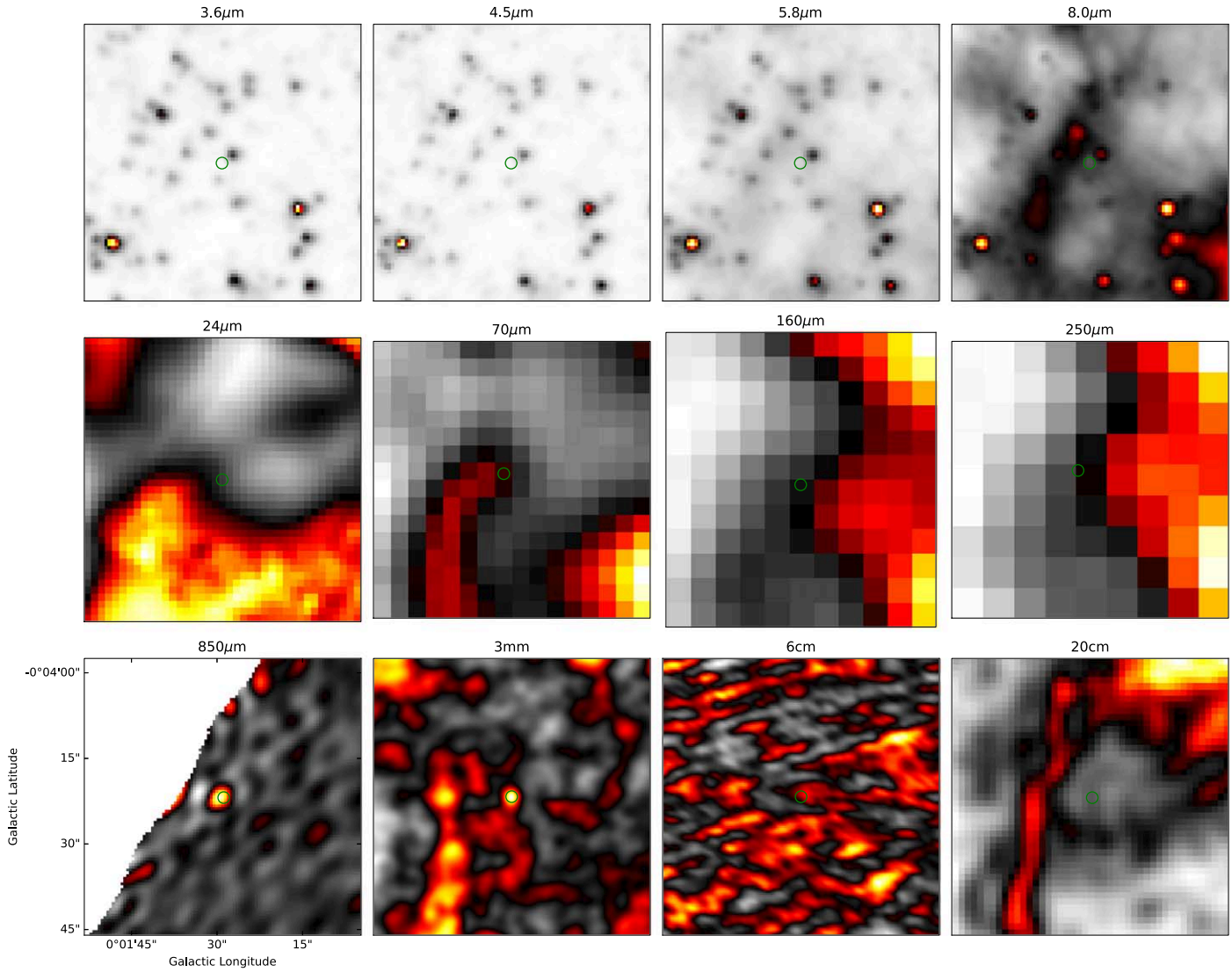

Figure 12. Continuum images of the cutout region at several wavelengths as labeled. The cutout is centered on the source ICRS coordinates 17:45:57.75–28:57:10.77 and is 35″ on a side. The source location is indicated with a green circle, and it is only detected in the two ALMA bands. Top row: GLIMPSE (Churchwell et al. 2009). Middle row: MIPS (Carey et al. 2009) and Herschel (Traficante et al. 2011). Bottom row: ALMA (this work), VLA (Lu et al. 2019), and MEERKAT (Heywood et al. 2022).

(YSO) at infrared wavelengths. The nondetection at wavelengths short of 850 μm suggests either that there is a very optically thick dust envelope or that the driving source is low-mass and low-luminosity.

5. The source appears isolated, with no surrounding sources at any wavelength and very little surrounding cloud material. YSOs are not often found in such environments.
6. High-velocity outflows are expected to produce high-velocity shocks in the dense ISM gas. The lack of SiO emission and the low inferred temperature both imply that there are no high-velocity shocks. This evidence is the most problematic for the protostellar outflow hypothesis.
7. Such massive (50 $M_\odot$), compact ($<10^4$ au) cores are rarely observed and are generally much hotter (e.g., Bonfand et al. 2017, 2024; Budaiev et al. 2024; Jeff et al. 2024).

A protostellar source is not strictly ruled out but is very unlikely.

6.1.3. Explosive Outflow

Could this be an explosive outflow at an early stage analogous to Orion BN/KL (e.g., Bally et al. 2015, 2017)?

For this hypothesis to hold, the explosion must be very young, with $t \approx 10^4\,\mathrm{au}/70\ \mathrm{km\ s^{-1}} \approx 700\,\mathrm{yr}$. An isotropic explosion is consistent with the line profile.

This hypothesis has several problems in common with the protostellar outflow hypothesis: there is little surrounding ISM, there is no associated infrared emission (especially near-infrared H_2 and [Fe II], which would show up in the K band), there is no shocked SiO emission, and the excitation temperature is very low. The Orion BN/KL outflow is bright in all of these features that are not detected toward the MUBLO.

6.1.4. Protostellar Inflow

Could this be a site where large amounts of material are inflowing toward a central, collapsing source? This hypothesis

explains the lack of infrared detection but otherwise fails to explain all the main observables. In particular, the huge line width is unexpected for a collapsing source unless it is extremely massive (see Section 6.4). We would also expect to see an accretion shock, which might be expected to produce hot line emission.

6.1.5. Protostellar Collision

Protostars are likelier to collide than their main-sequence counterparts. They are bloated during their early phases as they radiate away their gravitational energy, and they reside in a dissipative medium that can result in multiple systems inspiraling. A protostellar collision would appear similar to a later-stage stellar merger as described in Section 6.2.2. We defer further discussion to that section.

6.1.6. Prestellar Core Collision

Gas falls in along the Galactic bar at high velocity, impacting the CMZ at high speeds (Sormani & Barnes 2019; Gramze et al. 2023). If dense prestellar cores were to form along the Galactic bar's dust lanes and impact one another in the center of the Galaxy, the high observed velocity dispersion could be produced. However, in doing so, extremely strong shocks should occur; therefore, we would expect to see bright SiO emission. Furthermore, this scenario is intrinsically unlikely, as the freefall timescale for a prestellar core with half the mass of the MUBLO (assuming two equal-mass cores, the most conservative limit) is only 25 kyr, so these cores would have had to have formed extremely recently.

6.2. Evolved Star

Could this be some sort of evolved star, such as an asymptotic giant branch or red supergiant star with an extreme wind? These mass-losing stars are generally detected in emission from sulfur-bearing species (e.g., Omont et al. 1993). The main evidence against this hypothesis is the lack of an infrared source, though the lack of an SiO $v = 1$ maser in the ACES data is also weak evidence against the MUBLO being an evolved star (at least 15% of red supergiants exhibit SiO masers; Verheyen et al. 2012). These end-of-life stars are generally extremely luminous; the known red supergiants in the GC have observed K-band magnitudes $m_K < 6$ (Schultheis et al. 2020).

It is theoretically possible that one could be hidden by a very high column density of dust produced in its own wind, similar to the R Coronae Borealis stars and OH/IR red supergiants like VY CMa (Humphreys et al. 2024), or episodic mass loss leading to events like Betelgeuse's Great Dimming (Levesque & Massey 2020; Montargès et al. 2021), but the high column density required for this mechanism to completely block the star's infrared light would make the MUBLO unique. The required local extinction must be $A_K > 10$ for an $m_K = 6$ star to be undetected in the GALACTICNUCLEUS data (Nogueras-Lara et al. 2019); while this amount of dust is compatible with the observed millimeter-derived column density (Section 3.4), a $10^5\ L_\odot$ star would heat the dust well above the upper limit of $T_D < 50$ K (the protostar models discussed in Section 6.1 demonstrate this point).

VY CMa is a helpful reference case as perhaps the most extreme mass-losing supergiant star in the Galaxy. It is an $L \sim 2 \times 10^5\ L_\odot$ (Monnier et al. 1999) star with $M > 2.5 \times 10^{-4}\ M_\odot$ of circumstellar dust ($M > 2.5 \times 10^{-2}\ M_\odot$ of gas using our gas-to-dust ratio; O'Gorman et al. 2015, but see Kamiński 2019, who model dust mass as much as 100× higher). If we were to consider VY CMa as only a millimeter continuum source, it is similar to the MUBLO: its 350 GHz flux, scaled to a distance of 8 kpc, is 40 mJy (Kamiński et al. 2013; O'Gorman et al. 2015), within a factor of 2 of the MUBLO. Similarly, its 100 GHz flux (which we extrapolate from Figure B.1 of O'Gorman et al. 2015) scaled is 2 mJy, about what we measure. However, the dust temperatures they measure are >10× hotter than allowed by our observational limits. VY CMa is a bright IRAS source, with $S_{25\mu m} = 149$ Jy (scaled to $d = 8$ kpc; Helou & Walker 1988; Matsuura et al. 2014), which is >100× the Spitzer MIPS upper limit.

Additionally, the stars that produce the most dust in their winds tend to drive slower winds, while hotter stars that drive faster winds, compatible with the >70 km s^{-1} we observe, tend to have less massive winds (e.g., the fastest winds in a sample of mass-losing giants, VY CMa and IRC+10240, have FWHM $\sim$ 60 km s^{-1}, less than half of the MUBLO's; Kemper et al. 2003; Quintana-Lacaci et al. 2023). Most of the mass is in lower-velocity material, with $v_{max} < 40$ km s^{-1} (Quintana-Lacaci et al. 2023). The molecular winds in these sources are bright in SO, like the MUBLO, but comparably bright in SiO, which the MUBLO is not (Kamiński et al. 2013; Matsuura et al. 2014; Quintana-Lacaci et al. 2023).

The dust mass we infer requires a truly extreme star to reproduce. The only star we know of that has ejected $\sim 10\ M_\odot$ of matter outside of a supernova is η Carinae, whose great eruption produced $\sim 10\ M_\odot$ in only a few years. However, η Car bears no observational similarities to the MUBLO. It has narrow molecular lines (Bordiu et al. 2022) because most of the ejecta are ionized. The system is also far too bright; its distance-scaled flux is $S_{100\ GHz} \approx 3$ Jy (Morris et al. 2020), over 10^3× greater than the MUBLO.

6.2.1. (P)PN

Following along the evolved star route, could this be a star that has evolved past the point of nuclear burning, traveling into the PPN or PN phase? The PN hypothesis is unlikely, since there is no sign of ionized gas, but PPNe can be much higher density and cooler. The limited number of molecules detected could be a consequence of some peculiar enrichment process in the star, though we have no model for such a process.

The line width is one possible problem with this hypothesis. In observed PNe/PPNe, the core line width in molecular gas is generally small (e.g., CRL 618 has widths of $\sim$15 km s^{-1}; Lee et al. 2013a, 2013b). There are examples of broad lines, though: the Boomerang nebula has $\sim$100 km s^{-1} wide absorption from its fastest-expanding material seen in CO (Sahai et al. 2017). There are also many $\sim$150 km s^{-1} molecular jets detected among (P)PNe (Sahai & Patel 2015; Guerrero et al. 2020). These jets tend to be much fainter broad-wing components next to a central, more massive component, and in at least some cases they have coincident SiO, so the MUBLO would still stand out as unique, but there are analogs.

In one of the most extreme molecular PPN examples, I08005, which has 200 km s^{-1} wide CO and SiO lines, no continuum was detected at an upper limit of 1 mJy at 870 μm at a distance of 3 kpc (Sahai & Patel 2015). The detection of the MUBLO at 90 mJy at 8 kpc at the same wavelength makes it >400× brighter in the millimeter continuum than this PPN.

This difference suggests that the MUBLO is too dust-rich to be a PPN.

The lack of a detected continuum source at short wavelengths is again a problem for the PPN hypothesis. For a PN, we would not necessarily expect a central continuum source to be detectable in the infrared, but PPNe usually have fairly large stellar photospheres and are luminous in the infrared.

While there are some similarities between (P)PNe and the MUBLO, most of the evidence suggests that these are not the same class of object.

6.2.2. Stellar Merger: A Luminous Red Nova

Could the object be the result of stellar merger? Luminous red novae (LRN) are a class of transients thought to be associated with stellar mergers, and the MUBLO shares some observational features with the remnants of these events. Stellar mergers are expected to be more common in the high-density inner Galaxy and may even be the origin of the G objects near the GC (Ciurlo et al. 2020). Stellar mergers that produce LRN are often accompanied by high-velocity, cold molecular outflows (Kamínski et al. 2018). The energy released in stellar merger events can be $\sim 10^{48}$ erg (Retter et al. 2006), comparable to the energy in the MUBLO (Section 3.4), though the component in the molecular remnant of these mergers is $\sim 10^{46}$ erg (Kamínski et al. 2018). The very large energy in the molecular gas in the MUBLO, $E \sim 5 \times 10^{48}$ erg, suggests that a complete merger rather than a glancing collision is more likely; the gravitational energy in a merger of two solar-mass objects is 4×10^{48} erg.

Among the handful of known Galactic LRN, four with millimeter/submillimeter spectral line observations exhibit SO/SiO ratios ranging from 1 to 7, as reported in studies by Kamiński et al. (2015, 2018, 2020). These ratios are notably 2 orders of magnitude lower than the ratio observed toward the MUBLO. Gas temperature estimates from SiO, SO, and SO_2 for three of these four sources exceed $T > 50$ K, with Kamínski et al. (2018) identifying temperatures above 200 K in SO_2, which is substantially higher than the temperature estimates for the MUBLO. CK Vul, the oldest red nova, stands out as the only exception, with a temperature of 12 K. Therefore, the chemistry and excitation conditions of the MUBLO are different from the handful of known red novae.

We explore two examples, V838 Mon and CK Vul, in more detail.

V838 Monocerotis—V838 Mon exhibits some similarities to the MUBLO. ALMA observations of V838 Mon 17 yr after outburst reveal broad line widths, $v_{\rm FWHM} \approx 150$ km s^{-1}, in lines of CO, SO, SiO, and AlOH spread over $\sim$700 au (Kamínski et al. 2021b). The integrated intensity of the SO 5(6)–4(5) line in their data is $S \sim 9$ Jy km s^{-1}, which, if converted to a distance of 8 kpc, would drop to $\sim$4 Jy km s^{-1} ($d_{V838} = 5.9$ kpc), comparable to the observed integrated intensity of SO 2(3)–1(2) in the MUBLO (Table 3). However, they observe an SiO 5–4/SO 5(6)–4(5) ratio >2, while our object has SiO 2–1/SO 2(3)–1(2) < 0.02, implying that a dramatically different chemistry is present. The continuum observed toward V838 Mon at 1mm is $S \approx 2$ mJy (1 mJy at 8 kpc); for comparison, interpolating our observed flux between the B3 and B7 observations, the expected flux of the MUBLO is $S_{1\ \rm mm} = 30$ mJy, so about 30 times brighter.

V838 Mon is also a notably bright infrared source. From 2010 to 2020, it remained at $m_K \lesssim 5$ (Woodward et al. 2021), which would be roughly $m_K < 6$ at $d = 8$ kpc. The K-band upper limit from GALACTICNUCLEUS is about $m_K > 16$ (the 80% completeness limit; Nogueras-Lara et al. 2020), so $A_K > 10$ would be required to hide a central source like V838 Mon in the MUBLO (and extinction along the Galactic plane is only $A_K \sim 3$ toward the GC). In the mid-infrared, V838 Mon is bright, $S_{19.7\ \mu\rm m} = 38$ Jy (18 Jy at $d_{\rm GC}$), while the upper limit from Spitzer 24 μm toward the MUBLO is about 1.3 Jy, which requires $A_{24\ \mu\rm m} \approx 3$ to hide. At longer wavelengths, V838 Mon is fainter, and the limits from Herschel are less stringent.

CK Vulpecula—A second comparison source of interest is CK Vulpecula, an LRN that occurred in 1670. Unlike V838 Mon, its SED is a reasonable match to that of the MUBLO. It has long-wavelength fluxes that are comparable to those of the MUBLO; assuming $d_{\rm CK} = 3.2$ kpc (Banerjee et al. 2020; Kamiński et al. 2021a), its fluxes scaled to $d = 8$ kpc are $S_{100\ \rm GHz} \approx 2$ mJy, $S_{350\ \rm GHz} \approx 20$ mJy, $S_{24\ \mu\rm m} = 1.5$ mJy, and $S_{6\ \rm GHz} = 0.2$ mJy (Kamiński et al. 2015). The millimeter measurements are within a factor of a few of the MUBLO's measurements, and the others are consistent with the upper limits: CK Vul does not have a detected central source at infrared (<24 μm) wavelengths. The preferred SED model in Kamiński et al. (2015) has dust with $T = 15$ K and $\beta = 1$, with inferred central source luminosity[36] $L \approx 20\ L_\odot$, and these authors infer a total gas mass of $M = 1 M_\odot$ from their CO observations (they do not report a dust mass).

The key differences between CK Vul and the MUBLO are in its emission lines. All of the molecules seen in the MUBLO, SO, SO_2, and CS, are detected in CK Vul (Kamiński et al. 2020). However, the SO and SO_2 lines in CK Vul are $\gtrsim$10× fainter than the SiO lines that are not detected in the MUBLO, and several lines of SO seen in the MUBLO are not detected in CK Vul because they are swamped by transitions from other molecules, e.g., HC^{15}N, that are not present in the MUBLO (Kamiński et al. 2017). While there is significant emission in CK Vul with FWHM $\sim$ 100−200 km s^{-1} seen in CO and CS, the SO_2 lines are narrow, $\lesssim$50 km s^{-1} (Kamiński et al. 2020; SO is detected, but its line profile is not shown). The abundances of SO, SO_2, CS, SiO, and HC_3N are all roughly the same (equal within error bars) in CK Vul (Kamiński et al. 2020), in contrast to the MUBLO, where SO and SO_2 are much more abundant than SiO and HC_3N. In summary, while CK Vul is quite similar to the MUBLO in the continuum, it is dramatically different in molecular lines.

The stellar merger/LRN hypothesis seems quite plausible, but there remain several features that distinguish the MUBLO from other LRN. The dust mass is substantially larger, by more than an order of magnitude, than observed toward any other merger remnant. There is no hint of a central source at infrared wavelengths, making the MUBLO much more obscured than any previous LRN except CK Vul. The chemistry is dramatically different, with the MUBLO characterized by a lack of SiO. Together, these arguments imply that if the MUBLO is a merger remnant, it is from a merger of more massive stars than previously observed LRN (to account for the extra mass), and it occurred >10 yr ago to account for the re-

[36] Kamiński et al. (2015) reported $L = 1\ L_\odot$, but that work adopted $d_{\rm CK} = 0.7$ kpc; later works have all confirmed that it is more distant (Banerjee et al. 2020; Kamiński et al. 2021a).

freeze-out of SiO (but in old LRN, like CK Vul, SiO has not frozen out). The nova itself should have been extremely luminous, then, and have driven light echoes comparable to those created by V838 Mon—these might then be detectable in scattered light in the infrared if the event was recent enough.

6.3. High-velocity Compact Cloud

There have been many HVCCs reported in the GC region. These are peculiar clouds characterized by their compact sizes ($d \lesssim 5$ pc) and broad velocity widths ($\Delta V \gtrsim 50$ km s^{-1}). These have been explained as either material accelerated by supernova explosions, a connecting bridge between colliding clouds, or gas orbiting around invisible massive objects (Oka et al. 2014, 2016, 2022; Iwata et al. 2023). The MUBLO shares some properties with HVCCs, specifically the broad line width, but it is much smaller than the known HVCCs. All reported HVCCs have been found with single-dish telescopes and thus are extended over parsec scales, while the MUBLO has a radius smaller than $r < 5000$ au ($r < 0.02$ pc). Recent ALMA observations toward two HVCCs detected several unresolved ultracompact clumps with broad velocity width ($\Delta V \sim 50$ km s^{-1}; Takekawa et al. 2019; Iwata et al. 2023). These differ from the MUBLO in a few observational respects: their line widths are somewhat narrower, they are detected in different lines (CO, CH_3OH, SiO, HCN), they do not contain compact millimeter continuum sources, and they are surrounded by and connected to extended high-velocity-dispersion gas. They are therefore unlikely to be the same class of object.

6.4. Intermediate-mass Black Hole

Given the broad line width, it is possible that the MUBLO is comprised of gas in orbit around a very deep potential well. Because of the nondetection at multiple wavelengths, that potential well is dark, so a cluster of stars is an unlikely explanation. We therefore consider whether the object may be an IMBH (of order $10^4\ M_\odot$).

There have been many previous claims of IMBH detections in the CMZ (Oka et al. 2016; Tsuboi et al. 2017; Takekawa et al. 2019, 2020). These have been hard to confirm, since there exist many alternative explanations for broad-line-width gas (Oka et al. 2017; Ballone et al. 2018; Ravi et al. 2018; Tanaka 2018). We therefore approach this hypothesis cautiously, recognizing that significant evidence is required to claim that a black hole is the only acceptable explanation.

The velocity profile observed has a width that could be produced by an orbit around a central potential. An orbital velocity of 70–80 km s^{-1} (roughly the half-width of the MUBLO's line profile) would occur at 10^3–10^4 au for a few $10^4\ M_\odot$ black hole (see Figure 13). However, a disk with a pure Keplerian orbit seen edge-on should not produce a Gaussian profile but should instead produce a double-peaked profile with peaks corresponding to the disk's outermost radii. The peak of the SO profile is a key limit on this model, since it appears consistent with a smooth Gaussian (e.g., Figure 2). In order for the double-peaked profile to be obscured, either the purported disk would need to be face-on, which would reduce the observed line width, or the gas would need to be very turbulent. A very high degree of turbulence is plausible but would likely produce significant shocks; therefore, we would expect to see SiO emission.

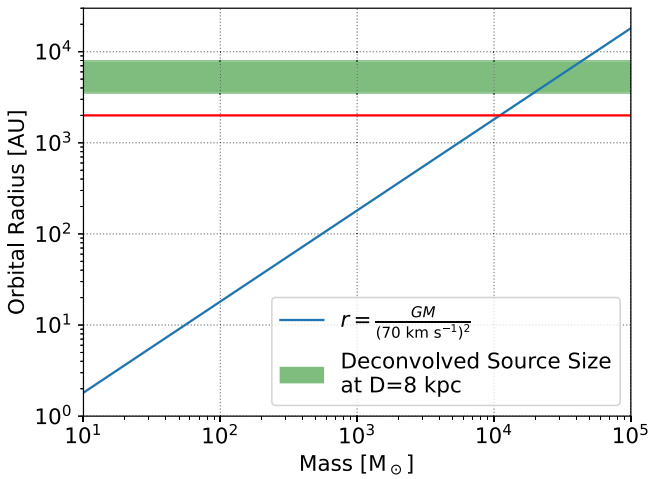

Figure 13. For the IMBH model, we plot $r = GM/v^2$ to obtain limits on the mass assuming the source is resolved (see Table 3). The green highlighted zone covers the range from the minor to major deconvolved source size. The red line at 2000 au shows the location of the fitted offset between the red and blue lobes of the SO line (Figure 5).

Alternatively, a lower-mass object would produce this broad line width at smaller radii. The apparent low optical depth of the SO and CS lines sets a lower limit on the radius: if we assume the lines are optically thin, the filling factor must be ff > 0.1 (Section 3.1), limiting the radius to $r > 1400$ au, which implies a lower mass limit $M_{\rm BH} > 8000\ M_\odot$ following Figure 13. This is not a strict limit, however, as the line profile would not necessarily appear non-Gaussian for moderate optical depth; more detailed modeling would be needed to produce a firm lower limit.

Despite the apparent problems with a disk model, we explore it a bit further. We assume a central mass $M = 10^4\ M_\odot$ such that the orbital velocity reaches ~70 km s^{-1} at around 2000 au. We adopt a simple viscous disk model with $\alpha = 0.001$ and total mass $50\ M_\odot$, which results in surface density $\Sigma = 7 \times 10^{25}$cm^{-2} and Planck mean opacity $\kappa = 3$ cm^2 g^{-1}. The midplane temperature is then (Krumholz 2015, problem set 4)

$$T_m = \left[\frac{27\alpha k_B \Sigma^2 \kappa \Omega}{64 m \sigma_{SB}}\right]^{1/3}, \quad (3)$$

which we parameterize as

$$T_m = 7.3\ \mathrm{K} \left[\frac{M}{50\ M_\odot}\right]^{2/3} \left[\frac{\kappa}{3\ \mathrm{cm^2\ g^{-1}}}\right]^{1/3} \left[\frac{\alpha}{10^{-3}}\right]^{1/3} \times \left[\frac{r}{2000\ \mathrm{au}}\right]^{-4/3}. \quad (4)$$

This temperature is within a plausible range to explain the observed $T_{\rm LTE} \approx 13$ K, though it may imply either higher α, a smaller emitting radius, or perhaps that some other heating source is present (e.g., cosmic rays). We also compute the inner radius $r_{\rm min} = 9$ au by inverting Equation (4) and assuming $T_{\rm max} < 10^4$ K, since there is no detected ionized gas in the centimeter continuum or in recombination lines. The inner radius at which we would expect to detect molecular lines is roughly the dust destruction radius, $T \approx 2000$ K, at $r = 30$ au.

Additionally, we checked the stellar kinematics in the vicinity of our target source. Shahzamanian et al. (2022)

reported proper motions measured using the GALACTICNUCLEUS data. Within a few arcseconds of this object, there are several measured proper motions, but there is no apparent trend; in particular, there is no increase of proper motion closer to the source. This lack is not evidence for or against the IMBH hypothesis, though, as most stars in the field of view are likely at a large physical distance from the MUBLO despite their small projected distance.

While there are several appealing features of the IMBH model, in its simplest form, it does not explain all of the observed features of the MUBLO. We regard it as a possible explanation but do not favor it above other models.

6.5. Galaxy

Could this object be a background galaxy?

Assuming we have correctly identified the spectral lines in Section 3.1, the line-of-sight velocity of 40 km s^{-1} makes a background galaxy hypothesis very unlikely. There are few galaxies at this redshift (i.e., near zero), and these galaxies occupy a low density on the sky. If the MUBLO were a galaxy, we would be observing a very compact component of it, perhaps the center. Assuming a size scale of the center of $r \sim 100$ pc, in order to be unresolved at 1″ resolution, it would need to be at $D \gtrsim 20$ Mpc. At that distance, the expected redshift is $H_0 D \sim 1400$ km s^{-1}, such that the required peculiar velocity for this to be a galaxy would be ~ -1300 km s^{-1}, much larger than expected in the local neighborhood.

The observed chemistry is also evidence against this being a galaxy. We compare the MUBLO to the entire CMZ: taking the average over the whole of the GC from ACES TP observations, our CMZ has an average CS 2–1 brightness of 53 K km s^{-1} and SO 2(3)–1(2) brightness of 10 K km s^{-1}. Table 2 shows that the MUBLO has SO 2(3)–1(2)/CS 2–1 of about 1.8, while the CMZ has a ratio of 0.19, about a 10× difference. This other hypothetical CMZ would have to exhibit a dramatically different chemistry from our own. The HC_3N/CS brightness ratio in the MUBLO is $R < 0.04$, while the measured value in the CMZ is 0.11 from both our measurements and Jones et al. (2012), which is also a discrepancy but not quite as difficult to reconcile as the SO/CS ratio.

Given that a correct identification of the lines essentially rules out a background galaxy, could we have misidentified the lines? This possibility is entirely ruled out, as we have identified several lines of SO and its ^{34}S isotopologue in addition to a CS and C^{34}S line. While any one line could be misidentified, a grouping of five different lines redshifting exactly on top of the rest frequencies of lines of another species is exceedingly unlikely.

6.6. Supernova

Could this be the remnant of a star that went supernova, or perhaps even a failed supernova? A supernova would readily explain the lack of an infrared source, since the purported source would have exploded.

There is at least one recent example of a "failed supernova" candidate in which a source remained afterward but was highly reddened and fainter (Adams et al. 2017; Beasor et al. 2024; Kochanek et al. 2024). As far as we are aware, though, there are no millimeter-wavelength observations of N6946-BH1, so we cannot (yet) make a direct comparison between it and the MUBLO.

The presence of molecules is somewhat compatible with a supernova. SN 1987A exhibits molecular emission in CO and SiO with widths of ∼1000 km s^{-1} (Cigan et al. 2019). If the MUBLO is an SNR, it is both much narrower in line width and chemically distinct from SN 1987A. Under the SNR hypothesis, we should probably adopt a much lower gas-to-dust ratio such that the total mass of the MUBLO is $\lesssim 1\ M_\odot$. As explained in Section 4.4, recent work suggests the presence of dust mass reservoirs of $\sim 0.5\ M_\odot$ in some SNRs, underlining this point.

There is weak circumstantial evidence from the morphology of the surrounding material that there was an explosive event at the MUBLO's location. The gap between the 50 km s^{-1} cloud and the three little pigs (Figure 9) could be produced by a supernova, in principle. The MEERKAT and Chandra images of the area give no hint of an SNR, though, so if this was a supernova-driven cavity, its hot gas has already disappeared. Additionally, the size scale of the apparent gap is several parsecs, while the MUBLO's molecular emission is only a few thousand au, which is difficult to reconcile.

Supernovae are comprised of fast-moving ejecta and therefore should expand over time. The line width and the molecular and dust continuum intensity have all stayed roughly constant from 2012 to 2022 (Section 3.4). It is not clear how a supernova scenario would explain the steadiness of the observed dispersion over this ∼10 yr period. It is possible that we are seeing only the inner remnant that has been confined by the reverse shock.

In summary, we cannot rule out an SNR as an explanation for the MUBLO, but such a model does not account for all of its features.

7. Conclusion

We found a source exhibiting extremely high velocity dispersion, which we call a MUBLO. We do not have a conclusive classification of this source. Several hypotheses produce many of the observed features, but none explain them all.

The key observational features of the MUBLO are as follows.

1. It has a large line width (FWHM = 160 km s^{-1}, σ = 70 km s^{-1}) in molecular lines (SO and CS).
2. It is likely in the GC, since the broad lines show absorption from GC clouds.
3. It is compact, $\theta_{\rm FWHM,maj} < 1''$ ($\lesssim$8000 au assuming a distance of 8 kpc).
4. Its chemistry is unlike that of other known objects: the ratio of SO to CS and of SO and CS to other molecules is different from other GC and Galactic disk clouds and from evolved stars and stellar merger remnants. Most significant is the nondetection of SiO, which is a strong indication that there are no shocks in the MUBLO.
5. It is dusty, as evidenced by the spectral index of its continuum emission from 3 mm to 850 μm, $\alpha = 3.25$.
6. It is likely massive, with $M_{\rm gas} \sim 50\ M_\odot$ assuming typical ISM dust and a gas-to-dust ratio of 100, and therefore dense.
7. It is cold, $T_{\rm gas} \sim 15$ K and $T_{\rm dust} < 50$ K.
8. No counterpart is found at other wavelengths for which comparable resolution data exist, including infrared (1–25 μm), radio ($\lambda > 3$ mm), and X-ray (2–10 keV).

Given these observational features, we considered many physical explanations of the MUBLO. Among the most promising for follow-up are the stellar merger and IMBH hypotheses. There are no exact analogs to the MUBLO among known astronomical objects. Future mid-infrared and millimeter observations will be needed to determine what this object is.

Acknowledgments

We thank the anonymous referee for a helpful and constructive review. We thank Brett McGuire, Andres Izquierdo, Joel Kastner, and Elias Aydi for conversations about chemistry, disks, evolved stars, and novae that motivated some of the discussion sections. A.G. acknowledges support from the NSF under grants AAG 2008101, 2206511, and CAREER 2142300. The authors acknowledge University of Florida Research Computing for providing computational resources and support that have contributed to the research results reported in this publication. K.M.D. and S.V. are funded by the European Research Council (ERC) Advanced Grant MOPPEX 833460.vii. X.L. acknowledges support from the National Key R&D Program of China (No. 2022YFA1603101), the Natural Science Foundation of Shanghai (No. 23ZR1482100), the National Natural Science Foundation of China (NSFC) through grant Nos. 12273090 and 12322305, and the Chinese Academy of Sciences (CAS) "Light of West China" Program (No. xbzgzdsys-202212). L.C., I.J.S., and V.M.R. acknowledge funding from grant Nos. PID2019-105552RB-C41 and PID2022-136814NB-I00 by the Spanish Ministry of Science, Innovation and Universities/State Agency of Research MICIU/AEI/10.13039/501100011033 and by ERDF, UE. V.M.R. also acknowledges support from grant No. RYC2020-029387-I funded by MICIU/AEI/10.13039/501100011033 and by "ESF, Investing in your future," and from the Consejo Superior de Investigaciones Científicas (CSIC) and the Centro de Astrobiología (CAB) through the project 20225AT015 (Proyectos intramurales especiales del CSIC). R.S.K. acknowledges financial support from the European Research Council via the ERC Synergy Grant "ECOGAL" (project ID 855130), the German Excellence Strategy via the Heidelberg Cluster of Excellence (EXC 2181-390900948) "STRUCTURES," and the German Ministry for Economic Affairs and Climate Action in project "MAINN" (funding ID 50OO2206). A.S.-M. acknowledges support from the RyC2021-032892-I grant funded by MCIN/AEI/10.13039/501100011033 and by the European Union "Next GenerationEU"/PRTR, as well as the program Unidad de Excelencia María de Maeztu CEX2020-001058-M and support from PID2020-117710GB-I00 (MCI-AEI-FEDER, UE). C.B. gratefully acknowledges funding from the National Science Foundation under award Nos. 1816715, 2108938, 2206510, and CAREER 2145689, as well as from the National Aeronautics and Space Administration through the Astrophysics Data Analysis Program under award No. 21-ADAP21-0179 and through the SOFIA archival research program under award No. 09_ 0540. Q.Z. acknowledges the support of the National Science Foundation under award No. 2206512.

This Letter makes use of the following ALMA data: ADS/JAO.ALMA#2021.1.00172.L, ADS/JAO.ALMA#2012.1.00080.S, ADS/JAO.ALMA#2017.1.01185.S. ALMA is a partnership of ESO (representing its member states), NSF (USA) and NINS (Japan), together with NRC (Canada), NSTC and ASIAA (Taiwan), and KASI (Republic of Korea), in cooperation with the Republic of Chile. The Joint ALMA Observatory is operated by ESO, AUI/NRAO and NAOJ. The National Radio Astronomy Observatory is a facility of the National Science Foundation operated under cooperative agreement by Associated Universities, Inc.

Appendix A
TP Spectra

Figure 14 shows the ACES 12 m spectra with spectra from the TP (12 m single-dish) array overlaid. The TP peaks coincide with the dips in the 12 m spectra, indicating that the dips are caused by absorption lines either from foreground clouds or from interferometric imaging artifacts from resolved-out clouds. It is not possible to tell from the images whether the absorption is real or not, despite the clear absorption-line profile seen in Figure 1.

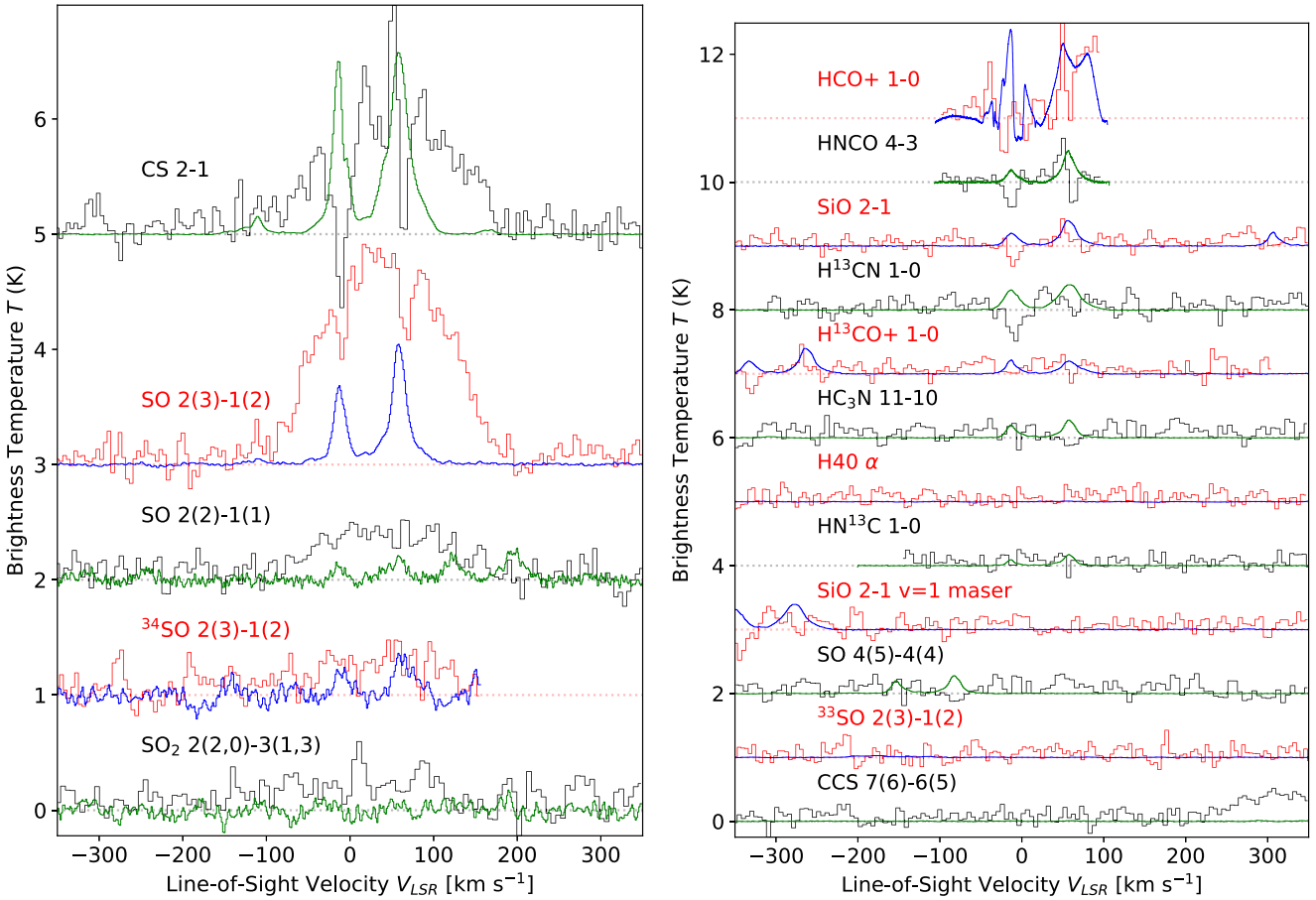

Figure 14. A repeat of Figure 2 with the TP data at this pointing, with $\sim 1'$ resolution, overlaid. For the detections (left), the TP data are scaled by factors of 1, 3, 10, 20, and 20 for CS, SO 2(3), SO 2(2), ^{34}SO 2(3), and SO_2, respectively. The overlap between the TP peaks and the 12 m array data dips confirms that the narrow features come from foreground molecular clouds.

Appendix B
Chemical Modeling

To guide our interpretation of the chemistry of the MUBLO, we use two types of astrochemical modeling codes: Meudon PDR (Le Petit et al. 2006) and UCLCHEM (Holdship et al. 2017). The former is a photochemical model of a 1D stationary PDR, and the latter is a 0D model that tracks the time evolution of the chemistry of a cloud.

The Meudon PDR code computes abundances of atoms and molecules and level excitation of any number of species at each position in the cloud (a stationary plane-parallel slab of gas and dust illuminated by a radiation field). The code solves the far-UV (FUV) radiative transfer at each point of the cloud, taking into account absorption in the continuum by dust and in discrete transitions by H and H_2. This model computes the thermal balance, taking into account heating processes (cosmic rays, photoelectric effects on grains, H_2 formation on grains, chemistry, grain–gas coupling, turbulence, photons, photodissociation and photoionization, and secondary photons) and cooling from discrete radiative transitions in IR and millimeter lines of various species following collisional excitation, free–free emission, and H_2 dissociation. A postprocessor code computes the line intensities and column densities.

The UCLCHEM code is a 0D model that follows the time evolution of the chemistry of a cloud. We use it to predict chemical abundances rather than intensities.

B.1. FUV and Cosmic-Ray Irradiation Models

We use the Meudon PDR code to model the MUBLO as a constant density cloud illuminated by the FUV radiation field (G_0). We adopt enhanced (compared to that in Galactic disk giant molecular clouds) H_2 CRIR (e.g., $\zeta_{CR} \approx (3.5 \pm 1.4) \times 10^{-16}$ s^{-1} for the LSR velocity range 20–75 km s^{-1} associated with the 50 km s^{-1} cloud; see Indriolo et al. 2015). Table 5 shows the input parameters. We accounted for the sulfur depletion usually needed in starless cores (a factor of >100) and that estimated in hot cores or bipolar outflows (a factor of $\sim$10; see Fuente et al. 2023, and references therein).

Figure 15 shows the model predictions of the SO-to-CS column density ratio, $N(SO)/N(CS)$, and the $I(SO\ 3_2\text{-}2_1)/I(CS\ 2\text{–}1)$ intensity ratio as function of the CRIR (ζ_{CR}). The blue shaded area represents the estimated and observed ratios, respectively (see Section 4.1 and Table 2). The estimated region comes from LTE modeling (Section 4.1), while the Meudon model performs non-LTE modeling of the line ratio, which is why the blue shaded regions are different for these two panels—i.e., the Meudon model suggests that the line ratio is not in LTE. These models show that a high density ($n_H \gtrsim 10^7$ cm^{-3}) is required to match the observations: when $n_H = 2 \times 10^5$ cm^{-3}, $N(SO)/N(CS)$ is larger than 20 for all ζ_{CR}. Hence, the computed intensity and column density ratios never overlap with the estimated ratio from Section 4.1.

Figure 16 shows the abundance and gas temperature profiles of a model with $n_H = 2 \times 10^7$ cm^{-3}, $\zeta_{CR} = 3 \times 10^{-15}$ s^{-1} per

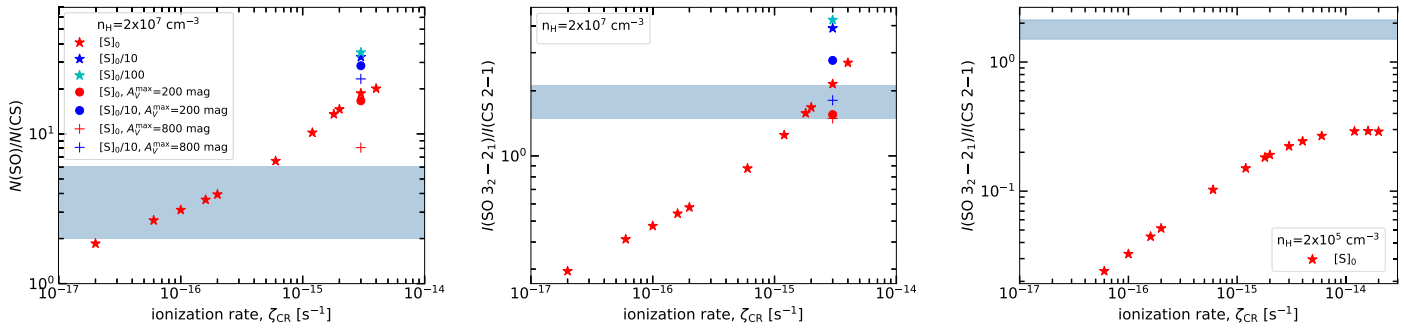

Figure 15. Meudon PDR model predictions for different values of ζ_{CR} (and fixed $G_0 = 10^3$, $n_H = 2 \times 10^7$ cm^{-3} (left and center) and $n_H = 2 \times 10^5$ cm^{-3} (right), and $A_{V,\,max} = 20$, 200, and 800 mag). Blue and cyan stars are the ratios in models with sulfur depleted 10 and 100 times. Red and blue dots are models with $A_V^{max} = 200$ mag and sulfur abundance [S]$_0$ and [S]$_0$/10, respectively. Red and blue plus signs are models with $A_V^{max} = 800$ mag and sulfur abundance [S]$_0$ and [S]$_0$/10, respectively. Left: markers show the SO vs. CS column density ratio. The blue horizontal shaded area represents the estimated column density ratio of ∼4 with a 50% uncertainty (see Section 4.1). Center and right: markers show the SO 3-2 to CS 2-1 intensity ratio. The blue horizontal shaded area represents the observed intensity ratio of ∼1.8 (see Table 2) with a 20% uncertainty.

Table 5
Input Parameters in the Meudon PDR Code

Parameter	Unit	Value	Note
n_H	cm^{-3}	2×10^5, 2×10^7	$n_H = n(H) + 2n(H_2)$, (1)
$A_{V,max}$	mag	20, 200, 800	(2), $L \sim$ 125, 1250, 5000 au
FUV radiation field, G_0	…	10^3	(3)
Cosmic-ray ionization rate, ζ_{CR}	s^{-1} per H_2	[2×10^{-17}, 2×10^{-14}]	(4), (5)
Dust extinction curve		Galaxy	(6)
R_V		3.1	(6)
$N_H/E(B-V) = C_D$	cm^{-2}	5.8×10^{21}	(7)
[S]	…	[S]$_0 \times$ (1, 0.1, 0.01)	[S]$_0 = 1.4 \times 10^{-5}$ (8), (9), (10)

Note. (1) See Section 4.2. (2) The relation between $A_{V,\,max}$ and the size of the computed cloud, L, in centimeters is $L = N_H/n_H = (C_D/n_H)(A_V/R_V)$. (3) Scaling parameter to the interstellar radiation field; Mathis et al. (1983). (4) Indriolo et al. (2015). (5) Le Petit et al. (2016). (6) Fitzpatrick & Massa (2007). (7) Bohlin et al. (1978). (8) Asplund et al. (2009). (9) Goicoechea & Cuadrado (2021). (10) Fuente et al. (2023).

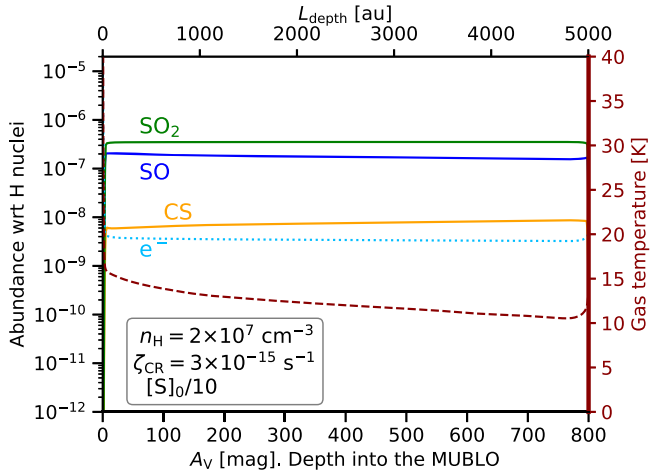

Figure 16. Abundance and T_k profiles of constant density gas-phase photochemical models with $n_H = 2 \times 10^7$ cm^{-3}, $\zeta_{CR} = 3 \times 10^{-15}$ s^{-1}, and sulfur abundance depleted by a factor of 10 (see blue plus signs in Figure 15).

H_2 molecule, and sulfur abundance depleted by a factor of 10. The gas temperature at large A_V is $T_k \sim$ 10–15 K, which agrees with the measured $T_{LTE} = T_{ex}$(SO).

In Section 3.1, we show that this source has an I(SO 3_2-2_1)/I(CS 2–1) ratio of about 1.8, while it has N(SO)/N(CS) of about 4, though the estimated N(CS) value is dominated by systematic uncertainty in T_{ex}. The model predictions result in a narrow range of parameters consistent with the observed SO/CS intensity ratio and estimated SO/CS column density ratio, $n_H \sim 2 \times 10^7$ cm^{-3} and $10^{-16} \lesssim \zeta_{CR} \lesssim 5 \times 10^{-15}$ s^{-1}.

B.2. UCLCHEM Models

We describe the UCLCHEM models run in this section. Table 6 shows the parameter grid we ran. We accounted for the observed depletion of silicon (Si; e.g., Savage & Sembach 1996) and sulfur (S; e.g., Palumbo et al. 1997) abundances by evaluating both a model with solar initial abundances and a model with a depletion of a factor of 10 for S and 100 for Si. For models with gas and dust temperatures set to 15 K (see Figure 17), we find that the observed ratio SO/SiO $\gtrsim$ 100 is predicted for densities $\leqslant 10^6$ cm^{-3}, while for the 50 K models (see Figure 18), the ratio can be recovered for all considered densities. SO/SiO > 100 is reachable for all considered CRIR and UV field strengths regardless of the gas and dust temperatures; however, in the case of the lowest-density scenario ($n = 10^5$ cm^{-3}) for the 50 K models, the ratio is only recovered after more than 10^7 yr. For the medium-density scenario, the ratio is quickly achieved and persists over a long chemical timescale. For the highest-density scenario, the ratio increases rapidly during the collapse, but once the final density is reached, both SiO and SO quickly freeze out.

Moreover, K. M. Dutkowska et al. (2024, in preparation) explored a wide range of continuous shock model parameters, covering shock velocity 5–30 km s^{-1}, preshock medium

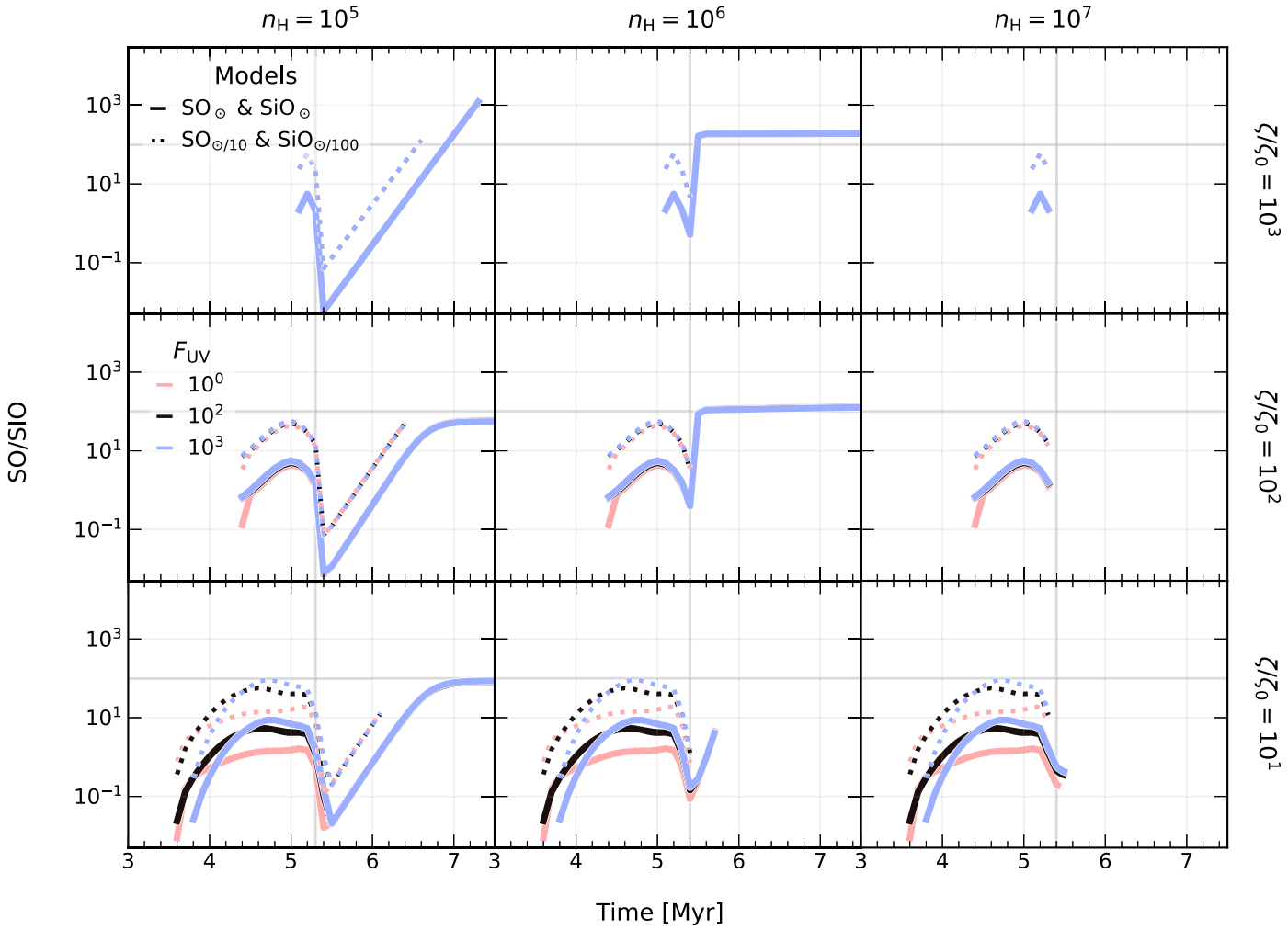

Figure 17. The evolution of the SO/SiO ratio in UCLCHEM models at a temperature of 15 K for both gas and dust. The parameters used in the models are detailed in Table 6. The ratio value of 100, which is the lower limit derived in Section 4.1, is represented by a thick horizontal gray line, while the vertical line indicates the time when the final density is reached. The ratio was calculated for time steps where both species are above the observable limit; i.e., their abundance is $\geqslant 10^{-12}$. For all models where the ratio of SO/SiO > 100, that ratio only occurs at late times, after the final density is reached. However, no models with a density of 10^7 cm^{-3}, in the rightmost column, can predict the observed ratio.

Table 6
Parameter Space Covered with UCLCHEM Models

Parameter	Unit	Values	Notes
$n_{H,final}$	cm^{-3}	10^5, 10^6, 10^7	$n_H = n(H) + 2n(H_2)$; $n_{H,\ init} = 10^2$ cm^{-3}
$T_{gas,dust}$	K	15, 50	⋯
ζ/ζ_0	⋯	10^1, 10^2, 10^3	$\zeta_0 = 1.310 \times 10^{-17}$ s^{-1}
F_{UV}	Habing	10^0, 10^2, 10^3	⋯
X(Si)	⋯	1.78^{-8}, $1.78^{-6\dagger}$	$^\dagger X(Si)_\odot$ (Jenkins 2009)
X(S)	⋯	3.51^{-7}, $3.51^{-6\dagger}$	$^\dagger X(S)_\odot$ (Jenkins 2009)

Note. The † symbols in the Values column indicate the source cited for the solar abundance in the Notes column.

temperature 15−35 K, preshock density 10^4−10^6 cm^{-3}, magnetic field 10^1−10^3 μG, CRIR 1.31×10^{-16}−1.31×10^{-13} s^{-1}, and UV irradiation 10^0−10^4 Habing. In these models, SO/SiO ratios are low, <100, during and shortly after the shock. The high SO/SiO ratio in the MUBLO is therefore either inherited from the collapse/quiescent cloud stage or achieved long after the shock has passed. Shocks with a velocity of $\leqslant 5$ km s^{-1} are the only ones capable of maintaining a ratio above 100. For a higher shock velocity, the SO/SiO ratio stays below 100, though given enough time after the shock, the SO/SiO ratio can eventually exceed 100 again.

Lastly, models at higher temperatures of 100 K and 150 K were simulated, since these higher temperatures are observed in the CMZ (Mills & Morris 2013; Ginsburg et al. 2016; Zeng 2018). For these models, an identical grid of models was run. These models reproduce the SO/SiO ratio only for

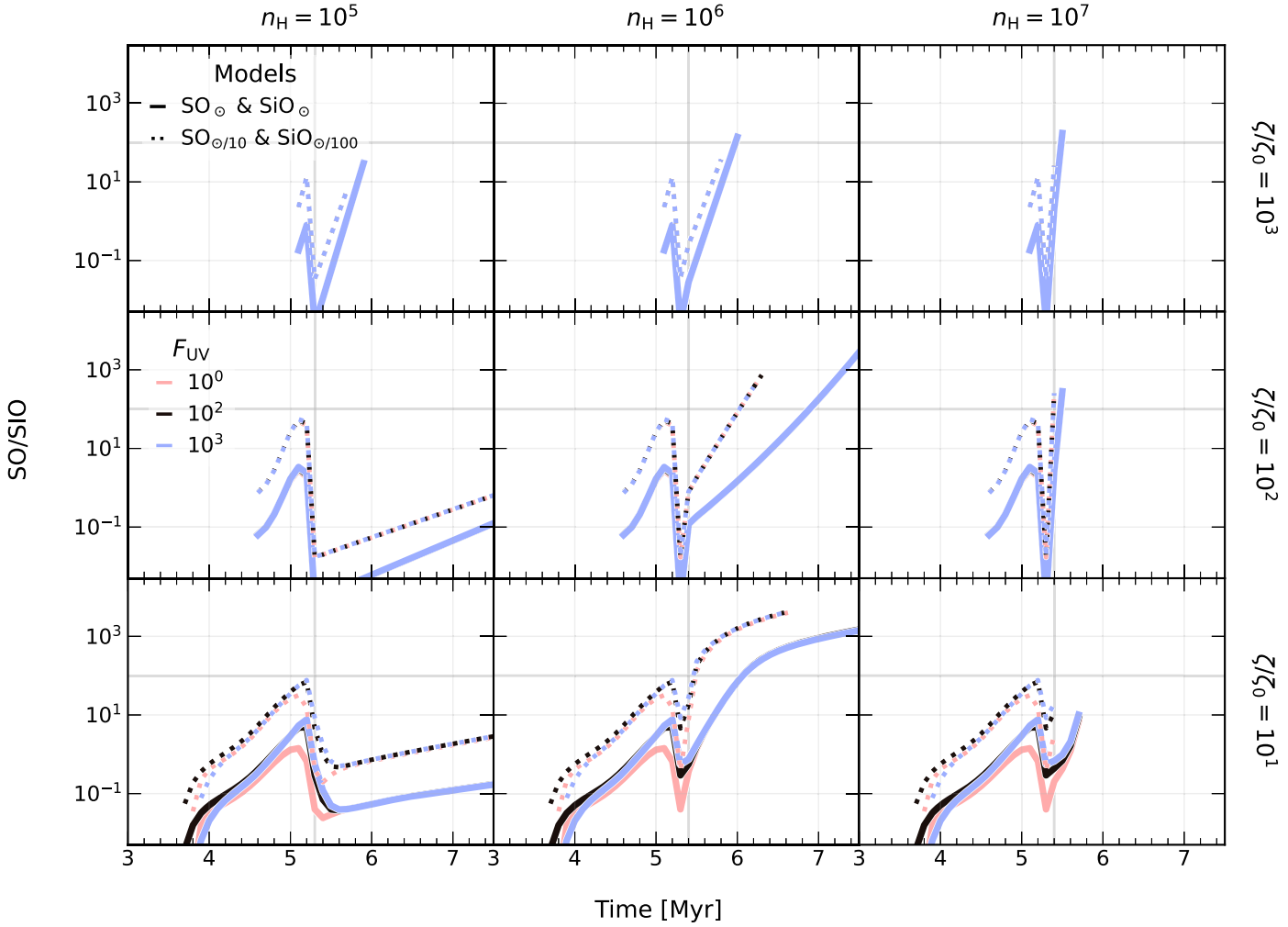

Figure 18. As in Figure 17 but for a temperature of 50 K. In this case, the ratio of SO/SiO is greater than 100 for all densities considered. However, for a density of 10^5 cm^{-3}, it takes a much longer time to reach the desired ratio, which exceeds the presented time range.

high CRIR, under which conditions the SiO is quickly destroyed and the SO reaches a steady state.

From these time-dependent gas-grain simulations, we conclude that a shock-free medium is favored to reproduce the high SO/SiO ratios. The ratios can be reproduced sufficiently by dense and possibly quiescent environments.

Appendix C
RADEX Models

We show parameter slices from the grid of RADEX models described in Section 4.2. The models use the large velocity gradient approximation with $dv = 70$ km s^{-1}. Figure 19 shows these model grids.

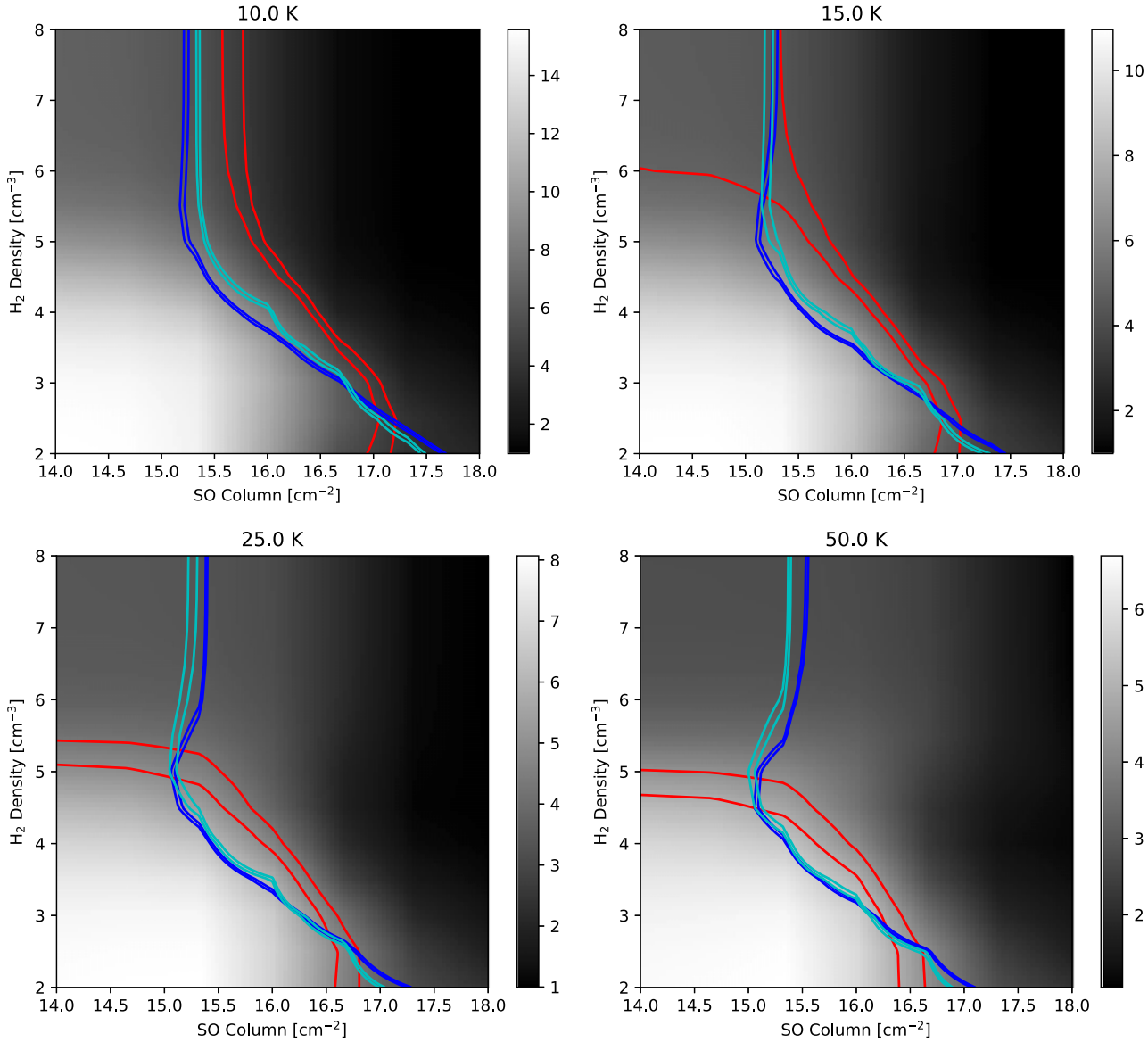

Figure 19. RADEX model grids used to constrain the temperature and density. Each plot shows in gray scale the ratio of the surface brightness of SO 2(3)–1(2) to SO 2(2)-1(1). The red contour shows the observationally allowed range, $R_{SO} = 4.87 \pm 0.33$. The cyan and blue contours show the allowed values for SO 2(2)–1(1) and SO 2(3)–1(2), respectively: $S_{2-1} = 0.38 \pm 0.02$ K and $S_{3-2} = 1.87 \pm 0.03$ K. The parameter space up and to the right (higher density and column density) of the blue curves and within the red curves is also allowed if the filling factor is ff < 1.

ORCID iDs

Adam Ginsburg https://orcid.org/0000-0001-6431-9633
John Bally https://orcid.org/0000-0001-8135-6612
Ashley T. Barnes https://orcid.org/0000-0003-0410-4504
Cara Battersby https://orcid.org/0000-0002-6073-9320
Nazar Budaiev https://orcid.org/0000-0002-0533-8575
Natalie O. Butterfield https://orcid.org/0000-0002-4013-6469
Paola Caselli https://orcid.org/0000-0003-1481-7911
Laura Colzi https://orcid.org/0000-0001-8064-6394
Katarzyna M. Dutkowska https://orcid.org/0000-0003-0980-6871
Pablo García https://orcid.org/0000-0002-8586-6721
Savannah Gramze https://orcid.org/0000-0002-1313-429X
Jonathan D. Henshaw https://orcid.org/0000-0001-9656-7682
Yue Hu https://orcid.org/0000-0002-8455-0805
Desmond Jeff https://orcid.org/0000-0003-0416-4830
Izaskun Jiménez-Serra https://orcid.org/0000-0003-4493-8714
Jens Kauffmann https://orcid.org/0000-0002-5094-6393
Ralf S. Klessen https://orcid.org/0000-0002-0560-3172
Emily M. Levesque https://orcid.org/0000-0003-2184-1581
Steven N. Longmore https://orcid.org/0000-0001-6353-0170
Xing Lu https://orcid.org/0000-0003-2619-9305
Elisabeth A. C. Mills https://orcid.org/0000-0001-8782-1992
Mark R. Morris https://orcid.org/0000-0002-6753-2066
Francisco Nogueras-Lara https://orcid.org/0000-0002-6379-7593
Tomoharu Oka https://orcid.org/0000-0002-5566-0634
Jaime E. Pineda https://orcid.org/0000-0002-3972-1978
Thushara G. S. Pillai https://orcid.org/0000-0003-2133-4862

Víctor M. Rivilla https://orcid.org/0000-0002-2887-5859
Álvaro Sánchez-Monge https://orcid.org/0000-0002-3078-9482
Miriam G. Santa-Maria https://orcid.org/0000-0002-3941-0360
Mattia C. Sormani https://orcid.org/0000-0001-6113-6241
Grant R. Tremblay https://orcid.org/0000-0002-5445-5401
Gijs Vermariën https://orcid.org/0000-0002-4346-5858
Alexey Vikhlinin https://orcid.org/0000-0001-8121-0234
Serena Viti https://orcid.org/0000-0001-8504-8844
Q. Daniel Wang https://orcid.org/0000-0002-9279-4041
Fengwei Xu https://orcid.org/0000-0001-5950-1932
Qizhou Zhang https://orcid.org/0000-0003-2384-6589

References

Adams, S. M., Kochanek, C. S., Gerke, J. R., Stanek, K. Z., & Dai, X. 2017, MNRAS, 468, 4968
Asplund, M., Grevesse, N., Sauval, A. J., & Scott, P. 2009, ARA&A, 47, 481
Ballone, A., Mapelli, M., & Pasquato, M. 2018, MNRAS, 480, 4684
Bally, J., Ginsburg, A., Arce, H., et al. 2017, ApJ, 837, 60
Bally, J., Ginsburg, A., Silvia, D., & Youngblood, A. 2015, A&A, 579, A130
Banerjee, D. P. K., Geballe, T. R., Evans, A., et al. 2020, ApJL, 904, L23
Barnes, A. T., Longmore, S. N., Battersby, C., et al. 2017, MNRAS, 469, 2263
Battersby, C., Keto, E., Walker, D., et al. 2020, ApJS, 249, 35
Beasor, E. R., Hosseinzadeh, G., Smith, N., et al. 2024, ApJ, 964, 171
Bianchi, S., & Schneider, R. 2007, MNRAS, 378, 973
Bohlin, R. C., Savage, B. D., & Drake, J. F. 1978, ApJ, 224, 132
Bonfand, M., Belloche, A., Menten, K. M., Garrod, R. T., & Müller, H. S. P. 2017, A&A, 604, A60
Bonfand, M., Csengeri, T., Bontemps, S., et al. 2024, arXiv:2402.15023
Bordiu, C., Rizzo, J. R., Bufano, F., et al. 2022, ApJL, 939, L30
Budaiev, N., Ginsburg, A., Jeff, D., et al. 2024, ApJ, 961, 4
Carey, S. J., Noriega-Crespo, A., Mizuno, D. R., et al. 2009, PASP, 121, 76
Chawner, H., Marsh, K., Matsuura, M., et al. 2019, MNRAS, 483, 70
Churchwell, E., Babler, B. L., Meade, M. R., et al. 2009, PASP, 121, 213
Cigan, P., Matsuura, M., Gomez, H. L., et al. 2019, ApJ, 886, 51
Ciurlo, A., Campbell, R. D., Morris, M. R., et al. 2020, Natur, 577, 337
Dame, T. M., & Thaddeus, P. 2008, ApJL, 683, L143
Dong, H., Wang, Q. D., Cotera, A., et al. 2011, MNRAS, 417, 114
Draine, B. T. 2006, ApJ, 636, 1114
Draine, B. T., & Lee, H. M. 1984, ApJ, 285, 89
Fitzpatrick, E. L., & Massa, D. 2007, ApJ, 663, 320
Fuente, A., Rivière-Marichalar, P., Beitia-Antero, L., et al. 2023, A&A, 670, A114
Ginsburg, A., Henkel, C., Ao, Y., et al. 2016, A&A, 586, A50
Ginsburg, A., Anderson, L. D., Dicker, S., et al. 2020, ApJS, 248, 24
Goicoechea, J. R., & Cuadrado, S. 2021, A&A, 647, L7
Gramze, S. R., Ginsburg, A., Meier, D. S., et al. 2023, ApJ, 959, 93
Guerrero, M. A., Suzett Rechy-García, J., & Ortiz, R. 2020, ApJ, 890, 50
Helou, G., & Walker, D. W. 1988, Infrared Astronomical Satellite (IRAS) Catalogs and Atlases: The Small Scale Structure Catalog, 7
Henshaw, J. D., Barnes, A. T., Battersby, C., et al. 2023, ASP Conf. Ser. 534, Protostars and Planets VII, ed. S. Inutsuka, (San Francisco, CA: ASP), 83
Heywood, I., Rammala, I., Camilo, F., et al. 2022, ApJ, 925, 165
Holdship, J., Viti, S., Jiménez-Serra, I., Makrymallis, A., & Priestley, F. 2017, AJ, 154, 38
Hopkins, P. F. 2014, ApJ, 797, 59
Humire, P. K., Thiel, V., Henkel, C., et al. 2020, A&A, 642, A222
Humphreys, R. M., Richards, A. M. S., Davidson, K., et al. 2024, AJ, 167, 94
Indriolo, N., Neufeld, D. A., Gerin, M., et al. 2015, ApJ, 800, 40
Iwata, Y., Oka, T., Takekawa, S., Tsujimoto, S., & Enokiya, R. 2023, ApJ, 950, 25
Jeff, D., Ginsburg, A., Bulatek, S., Tsujimoto, S., & Enokiya, R. 2024, ApJ, 962, 48
Jenkins, E. B. 2009, ApJ, 700, 1299
Jones, P. A., Burton, M. G., Cunningham, M. R., et al. 2012, MNRAS, 419, 2961
Kamiński, T. 2019, A&A, 627, A114
Kamiński, T., Gottlieb, C. A., Young, K. H., Menten, K. M., & Patel, N. A. 2013, ApJS, 209, 38
Kamiński, T., Menten, K. M., Tylenda, R., et al. 2015, Natur, 520, 322
Kamiński, T., Menten, K. M., Tylenda, R., et al. 2017, A&A, 607, A78
Kamiński, T., Menten, K. M., Tylenda, R., et al. 2020, A&A, 644, A59
Kamiński, T., Steffen, W., Bujarrabal, V., et al. 2021a, A&A, 646, A1
Kamínski, T., Steffen, W., Tylenda, R., et al. 2018, A&A, 617, A129
Kamínski, T., Tylenda, R., Kiljan, A., et al. 2021b, A&A, 655, A32
Kemper, F., Stark, R., Justtanont, K., et al. 2003, A&A, 407, 609
Kochanek, C. S., Neustadt, J. M. M., & Stanek, K. Z. 2024, ApJ, 962, 145
Krumholz, M. R. 2015, arXiv:1511.03457
Le Petit, F., Nehmé, C., Le Bourlot, J., & Roueff, E. 2006, ApJS, 164, 506
Le Petit, F., Ruaud, M., Bron, E., et al. 2016, A&A, 585, A105
Lee, C.-F., Sahai, R., Sánchez Contreras, C., Huang, P.-S., & Hao Tay, J. J. 2013a, ApJ, 777, 37
Lee, C.-F., Yang, C.-H., Sahai, R., & Sánchez Contreras, C. 2013b, ApJ, 770, 153
Levesque, E. M., & Massey, P. 2020, ApJL, 891, L37
Longmore, S. N., Bally, J., Testi, L., et al. 2013, MNRAS, 429, 987
Lu, X., Mills, E. A. C., Ginsburg, A., et al. 2019, ApJS, 244, 35
Mathis, J. S., Mezger, P. G., & Panagia, N. 1983, A&A, 128, 212
Matsuura, M., Yates, J. A., Barlow, M. J., et al. 2014, MNRAS, 437, 532
Mills, E. A. C., & Morris, M. R. 2013, ApJ, 772, 105
Molinari, S., Swinyard, B., Bally, J., et al. 2010, A&A, 518, L100
Monnier, J. D., Tuthill, P. G., Lopez, B., et al. 1999, ApJ, 512, 351
Montargès, M., Cannon, E., Lagadec, E., et al. 2021, Natur, 594, 365
Morris, M., & Serabyn, E. 1996, ARA&A, 34, 645
Morris, P. W., Charnley, S. B., Corcoran, M., et al. 2020, ApJL, 892, L23
Muno, M. P., Bauer, F. E., Baganoff, F. K., et al. 2009, ApJS, 181, 110
Nogueras-Lara, F., Gallego-Calvente, A. T., Dong, H., et al. 2018, A&A, 610, A83
Nogueras-Lara, F., Schödel, R., Gallego-Calvente, A. T., et al. 2019, A&A, 631, A20
Nogueras-Lara, F., Schödel, R., Gallego-Calvente, A. T., et al. 2020, NatAs, 4, 377
Ochsenbein, F., Bauer, P., & Marcout, J. 2000, A&AS, 143, 23
O'Gorman, E., Vlemmings, W., Richards, A. M. S., et al. 2015, A&A, 573, L1
Oka, T., Mizuno, R., Miura, K., & Takekawa, S. 2016, ApJL, 816, L7
Oka, T., Tanaka, K., Matsumura, S., et al. 2014, in IAU Symp. 303, The GC: Feeding and Feedback in a Normal Galactic Nucleus (Cambridge: Cambridge Univ. Press), 202
Oka, T., Tsujimoto, S., Iwata, Y., Nomura, M., & Takekawa, S. 2017, NatAs, 1, 709
Oka, T., Uruno, A., Enokiya, R., et al. 2022, ApJS, 261, 13
Omont, A., Lucas, R., Morris, M., & Guilloteau, S. 1993, A&A, 267, 490
Ossenkopf, V., & Henning, T. 1994, A&A, 291, 943
Palumbo, M. E., Geballe, T. R., & Tielens, A. G. G. M. 1997, ApJ, 479, 839
Quintana-Lacaci, G., Velilla-Prieto, L., Agúndez, M., et al. 2023, A&A, 669, A56
Ramírez, S. V., Arendt, R. G., Sellgren, K., et al. 2008, ApJS, 175, 147
Ravi, V., Vedantham, H., & Phinney, E. S. 2018, MNRAS, 478, L72
Retter, A., Zhang, B., Siess, L., & Levinson, A. 2006, MNRAS, 370, 1573
Richardson, T., Ginsburg, A., Indebetouw, R., & Robitaille, T. P. 2024, ApJ, 961, 188
Robitaille, T. P. 2017, A&A, 600, A11
Sahai, R., & Patel, N. A. 2015, ApJL, 810, L8
Sahai, R., Vlemmings, W. H. T., & Nyman, L. . 2017, ApJ, 841, 110
Savage, B. D., & Sembach, K. R. 1996, ARA&A, 34, 279
Schultheis, M., Rojas-Arriagada, A., Cunha, K., et al. 2020, A&A, 642, A81
Shahzamanian, B., Schoedel, R., Nogueras-Lara, F., et al. 2022, A&A, 662, A11
Sormani, M. C., & Barnes, A. T. 2019, MNRAS, 484, 1213
Takekawa, S., Oka, T., Iwata, Y., Tsujimoto, S., & Nomura, M. 2019, ApJL, 871, L1
Takekawa, S., Oka, T., Iwata, Y., Tsujimoto, S., & Nomura, M. 2020, ApJ, 890, 167
Tanaka, K. 2018, ApJ, 859, 86
Tokuyama, S., Oka, T., Takekawa, S., et al. 2019, PASJ, 71, S19
Traficante, A., Calzoletti, L., Veneziani, M., et al. 2011, MNRAS, 416, 2932
Tsuboi, M., Kitamura, Y., Tsutsumi, T., et al. 2017, ApJL, 850, L5
Tsuboi, M., Miyazaki, A., & Okumura, S. K. 2009, PASJ, 61, 29
Uehara, K., Tsuboi, M., Kitamura, Y., Miyawaki, R., & Miyazaki, A. 2019, ApJ, 872, 121
van der Tak, F. F. S., Black, J. H., Schöier, F. L., Jansen, D. J., & van Dishoeck, E. F. 2007, A&A, 468, 627
Verheyen, L., Messineo, M., & Menten, K. M. 2012, A&A, 541, A36
Whitmore, B. C., Allam, S. S., Budavári, T., et al. 2016, AJ, 151, 134
Woodward, C. E., Evans, A., Banerjee, D. P. K., et al. 2021, AJ, 162, 183
Yan, Y. T., Henkel, C., Kobayashi, C., et al. 2023, A&A, 670, A98
Yu, H. Z., Zhang, J. S., Henkel, C., et al. 2020, ApJ, 899, 145
Zeng, S., Jiméz-Serra, I., Rivilla, V. M., et al. 2018, MNRAS, 478, 2962